JOURNAL OF GEOPHYSICAL RESEARCH, VOL. 94, NO. B2, PAGES 1867–1887, FEBRUARY 10, 1989

Numerical Models of Plinian Eruption Columns and Pyroclastic Flows

GREG A. VALENTINE AND KENNETH H. WOHLETZ

Los Alamos National Laboratory, Los Alamos, New Mexico

Numerical simulations of physical processes governing the large-scale dynamics of Plinian eruption columns reveal conditions contributing to column collapse and emplacement of pyroclastic flows. The simulations are based on numerical solution of the time-dependent, two-phase, compressible Navier-Stokes equations for jets in a gravitational field. This modeling effort is directed toward studying the steady discharge phase of eruptions in contrast to our previous models of the initial, unsteady blast phase. Analysis of 51 eruption models covers a wide range of vent exit pressures, inertial and buoyancy driving forces, and coupling of energy and momentum between gas and pyroclasts. Consideration of three dimensionless groups (Richardson and Rouse numbers and thermogravitational parameter) facilitates this analysis and defines conditions leading to column collapse. For eruptions with similar particle size characteristics, exit pressure ratios are also very important in determining column behavior; column behavior is much more sensitive to exit pressure ratio than to the density ratio between the column and the atmosphere. Model eruption columns with exit pressures exceeding atmospheric pressure have diamond-shaped patterns at their bases with internal dynamics that correspond closely to observations of overpressured jets in laboratory experiments. Collapsing fountains form pyroclastic flows that consist of low-concentration fronts, relatively thick heads, vortex development along the top surfaces, and rising clouds of buoyant ash. The presence of coarse-grained proximal deposits primarily reflects tephra size sorting within the eruption column before collapse, as opposed to that which occurs during lateral transport of the material in pyroclastic flows. The dynamics and particle behavior in the proximal zone around collapsing eruption columns is examined; the modeling indicates that flow within a few kilometers of a vent will be at its highest particle concentration relative to other parts of the flow field.

INTRODUCTION

This paper is the second in a series concerning the application of numerical solution of the time-dependent, nonlinear, multiphase hydrodynamics equations to explosive volcanic phenomena associated with Plinian eruptions. The first paper [*Wohletz et al.*, 1984] outlined an overall evolution of caldera-related eruptions. In this evolutionary sequence a dike of volatile-rich magma is catastrophically exposed to the atmosphere. The sudden exposure of a high-pressure magma to atmospheric pressure produces an initial phase of unsteady flow characterized by shocks propagating into the atmosphere and rarefactions propagating down the conduit. This initial phase of an eruption, during which ash is driven out of the vent and laterally across the landscape largely by the pressure fluctuations associated with blast waves, comes to an end with the development of steady discharge from the vent. The steady phase of explosive eruption is characterized by the development of ash plumes and pyroclastic flows. This paper is devoted to modeling the first few minutes of steady discharge.

In order to develop a perspective for our model results we briefly review previous modeling of steady eruption columns. Then we describe the hydrodynamics equations used in our models, followed by analysis of the 51 numerical experiments. Dimensionless ratios are used to analyze the effects of various forces on eruption dynamics. Finally, we discuss implications of the modeling for development of pyroclastic flows and associated depositional facies variations.

Previous Modeling

Modeling of explosive volcanic eruptions has evolved rapidly over the past 20 years as quantitative field techniques for the study of pyroclastic deposits have provided many new data. The fact that most large eruptions have not been witnessed and recorded has spurred modeling efforts to obtain an understanding of eruption processes responsible for various types of tephra deposits. With respect to Plinian eruptions, most modeling has been based upon entrainment theory of turbulent jets and plumes. In the first treatment of columns using this approach, *Wilson* [1976] uses a single-phase, incompressible, turbulent jet model from *Prandtl* [1954] with modifications to account for gravity and thermal effects of entrained particles. Wilson's treatment solves the equations for conservation of mass and momentum invoking Prandtl's empirical relations for the rate of entrainment of ambient air (reflected in the assumed rate of widening of the jet with height). In these models it is assumed that pressure in the column at any given elevation is equal to the local ambient pressure. *Sparks and Wilson* [1976] and *Sparks et al.* [1978] extended the turbulent plume treatment to include conditions under which entrainment of ambient air, which produces buoyancy in a column, is not sufficient to thrust the column higher by convection, and the column collapses at the top of the gas thrust (jet) region to form pyroclastic flows.

In an effort to quantify the dynamics of Plinian eruption columns in the convective thrust region, which comprises most of the height of Plinian column, *Settle* [1978] and *Wilson et al.* [1978] apply an empirical formula that is consistent with that of *Morton et al.* [1956] for incompressible, convective plumes. This approach involves a power law relationship between mass discharge rate and eruption column height, namely $H \propto D^{1/4}$, where H is the height of the column top and D is the mass discharge rate of magma. *Jakosky* [1986] raises some questions about this relation, suggesting that it may be somewhat fortuitous due to the simplifications involving the atmospheric lapse rate and the use of the visible cloud top instead of the mass-averaged cloud top for the value of H. *Sparks and Wilson* [1982] apply the same type of incompressible turbulent plume theory to the 1979 eruptions of Soufriere,

Paper number 88JB03773.
0148-0227/89/88JB-03773$05.00

using an empirical entrainment constant (similar to a mixing length). This approach is extended by *Wilson and Walker* [1987] to account for atmospheric wind, in an application to tephra dispersal; this work supports some of the reservations raised by *Jakosky* [1986]. *Sparks* [1986] refines the theory of eruption plumes within the framework of turbulent, incompressible convection and includes climatic effects. *Carey and Sparks* [1986] apply the refined theory to tephra dispersal.

Woods [1988] has provided a comprehensive and critical review of the models listed above and has pointed out some important inconsistencies in the physics calculated by these models. Woods presents a new model of steady flow Plinian eruption columns which, although it is similar in its basic approach, is more rigorous than previous models of *Wilson* [1976], *Sparks* [1986], and *Wilson and Walker* [1987]; it also has the added feature of an energy conservation expression. Woods' calculations, as in previous models, use a single-phase approximation, are one-dimensional, and do not account for compressible flow (i.e., there are no pressure terms in the momentum equation and pressure differences between the atmosphere and column are neglected). The *Woods* [1988] model makes use of the *Prandtl* [1954] jet theory in much the same manner as the *Wilson* [1976] model.

The May 18, 1980, blast at Mount St. Helens brought attention to the importance of compressible fluid dynamic processes in volcanic jets. With this focus, *Kieffer* [1981] applied experimentally observed jet dynamics to that eruption and discussed the effects of exit pressures that exceed local ambient pressure on jet structure. Such a jet is characterized by complex patterns of rarefaction waves and shocks. To explore such structures further, *Kieffer and Sturtevant* [1984] present results of laboratory experiments on single-phase (one material) jets that are thermodynamically similar to multiphase volcanic products within a single-phase (pseudogas) approximation scheme. These experiments provide important insight into effects of jet exit pressure and the ratio of mixture density to atmospheric density.

In summary, previous work on eruption columns consists of two general approaches. The first is to model the effects of turbulence (entrainment) and gravity but to simplify the thermodynamics of the flows. The second is to examine the thermodynamics of the flows but to neglect turbulence and gravity. Both approaches have essentially considered the flows as single-phase fluids with properties modified by the presence of particles. In an effort to close the gap between the two approaches, we have modeled in two dimensions the compressible, two-phase flow in a gravitational field; this approach addresses most of the extensions of eruption column models that were suggested by *Woods* [1988]. Although a crude approximation of turbulence effects is included, our approach does not strictly model turbulence and related diffusive processes. This next step awaits development of a theory of turbulent, two-phase, compressible flow.

We have used a significantly different approach to turbulence (hence entrainment) in our modeling efforts because we believe that the use of empirical entrainment theory, derived from incompressible flow experiments, may be unsatisfactory. This problem is due to the strong dependence of mixing upon Mach number in shear flows, namely, that entrainment rates decrease substantially with increasing Mach number [*Brown and Roshko*, 1974]. Basic similarity considerations show that it is not satisfactory to model volcanic eruption columns as incompressible flows neither theoretically nor in the laboratory. Column velocities of several hundreds of meters per second are typical of Plinian eruptions. *Kieffer and Sturtevant* [1984] show that with moderate solid particle concentrations, the sound speeds of the eruptive mixtures are less than several hundred meters per second. So, in general, the Mach number effect should not be neglected, and the full conservation of energy equation must be solved along with continuity and conservation of momentum to make a reasonable model.

THEORETICAL APPROACH

Governing Equations

A comprehensive review of mathematical and numerical techniques for multiphase flow is given by *Stewart and Wendroff* [1984]. The approach taken here is to solve the full set of two-phase, compressible Navier-Stokes equations for injection of a hot, particle-laden gas into a cool, density-stratified atmosphere. The geometry of the problem is shown in Figure 1. Each phase is modeled as a continuum, one being compressible (gas phase) and the other incompressible (solid phase), using the formulation given by *Harlow and Amsden* [1975]. In this situation the governing equations in vector form are

$$\frac{\partial}{\partial t}(\theta_s\rho_s) + \nabla\cdot(\theta_s\rho_s\mathbf{u}_s) = 0 \tag{1a}$$

$$\frac{\partial}{\partial t}(\theta_g\rho_g) + \nabla\cdot(\theta_g\rho_g\mathbf{u}_g) = 0 \tag{1b}$$

$$\frac{\partial}{\partial t}(\theta_s\rho_s\mathbf{u}_s) + \nabla\cdot(\theta_s\rho_s\mathbf{u}_s\mathbf{u}_s) = -\theta_s\nabla p + K_s(\Delta\mathbf{u}) + \theta_s\rho_s\mathbf{g} - \nabla\cdot\tau_s \tag{2a}$$

$$\frac{\partial}{\partial t}(\theta_g\rho_g\mathbf{u}_g) + \nabla\cdot(\theta_g\rho_g\mathbf{u}_g\mathbf{u}_g) = -\theta_g\nabla p + K_g(\Delta\mathbf{u}) + \theta_g\rho_g\mathbf{g} - \nabla\cdot\tau_g \tag{2b}$$

$$\theta_s\rho_s\left[\frac{\partial I_s}{\partial t} + \nabla\cdot(I_s\mathbf{u}_s) - I_s\nabla\cdot\mathbf{u}_s\right] = R_s - \tau_s{:}\nabla\mathbf{u}_s \tag{3a}$$

$$\theta_g\rho_g\left[\frac{\partial I_g}{\partial t} + \nabla\cdot(I_g\mathbf{u}_g) - I_g\nabla\cdot\mathbf{u}_g\right] = -p\nabla\cdot(\theta_g\mathbf{u}_g + \theta_s\mathbf{u}_s) + R_g + |K_g|(\Delta\mathbf{u})^2 - \tau_g{:}\nabla\mathbf{u}_g \tag{3b}$$

Subscripts s and g refer to the solid (pyroclast) and gas phases of the flow, respectively, θ is volume fraction of a given phase, ρ is the material density, $\mathbf{u}$ is velocity, p is the pressure of the gas phase, K is the momentum transfer (drag) function, $\mathbf{g}$ is the gravitational acceleration, τ is the viscous stress tensor, I is specific internal energy, and R is the interphase heat transfer. Finally, $\Delta\mathbf{u}$, the slip velocity, is given by $\Delta\mathbf{u} = \mathbf{u}_g - \mathbf{u}_s$.

Equations (1*a*) and (1*b*) are conservation of mass for the solid and gas phase, respectively. Equations (2*a*) and (2*b*) are conservation of momentum. In (2*a*), note that the pressure term represents the accelerating force on the particle phase due to the gas pressure gradient. Since the pyroclasts are assumed to be dispersed, with negligible particle-particle interactions, the pressure for the solid phase is negligible. For both phases, conservation of specific internal energy (equations (3*a*) and (3*b*)) includes effects of interphase heat transfer and viscous dissipation. In addition to these, the specific internal energy of the gas phase is influenced by pressure work and energy produced by interphase drag. The general numerical solution method for these equations is given by *Harlow and*

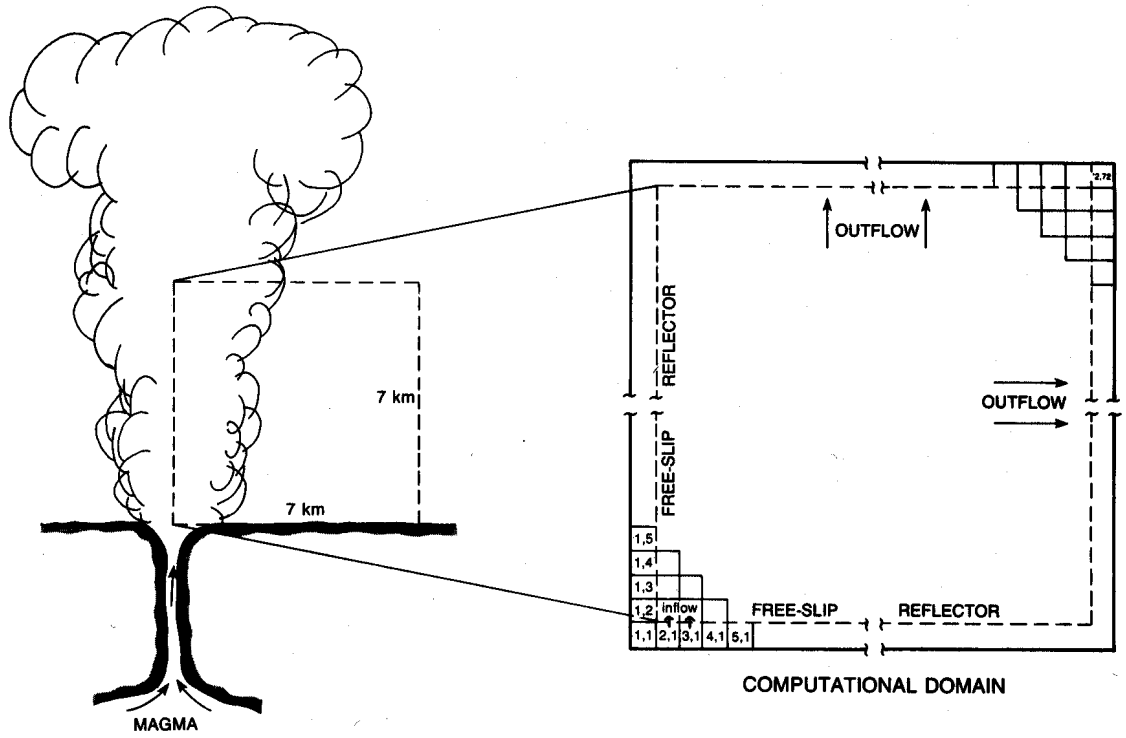

Fig. 1. Geometry of problem and the computational domain. The flow field is computed for a 7 × 7 km area above and laterally away from the vent, with the computational domain discretized into 100 × 100 m cells (toroids in three dimensions, because a cylindrical geometry is assumed) for finite difference approximation of equations (1)–(3). The outer "frame" of cells are used for specification of boundary conditions. See text for discussion.

Amsden [1975]; a specific example of the method is given by *Amsden and Harlow* [1974].

Equations (1)–(3) are very similar to those applied to the blast phase of explosive eruptions by *Wohletz et al.* [1984], with the exception of terms involving heat conduction within the gas phase and viscous effects. Scaling arguments that show intraphase heat conduction to be minor compared to other forms of energy transfer in (3*a*) and (3*b*) are summarized in the appendix. Building upon the modeling of *Wohletz et al.* [1984], we have included a stress tensor in the momentum and energy equations, which takes the form

$$\tau = -\theta\rho\nu \begin{bmatrix} 2\dfrac{\partial u}{\partial r} & 0 & \left[\dfrac{\partial v}{\partial r} + \dfrac{\partial u}{\partial z}\right] \\ 0 & 2\dfrac{u}{r} & 0 \\ \left[\dfrac{\partial v}{\partial r} + \dfrac{\partial u}{\partial z}\right] & 0 & 2\dfrac{\partial v}{\partial z} \end{bmatrix} \quad (4)$$

This expression is appropriate for two-dimensional cylindrical coordinates, r being the radial distance from the symmetry axis and z being vertical distance above the vent exit plane (simplified from *Bird et al.* [1960, p. 89]). Because the Reynolds number for these flows is very large ($\sim 10^{10}$ or larger, see the appendix), the contribution of stress from "molecular" viscosity (which is influenced by the presence of particles) is negligible. However, such high Reynolds numbers indicate that turbulence is likely in the flows, in which case it is necessary to consider turbulence-induced diffusion of transport quantities (mass, momentum, and energy).

As stated earlier, a detailed model of compressible, multiphase turbulence has not been developed, so as a crude approximation we have used a mixing-length approach to determining effective turbulence viscosity. This approach is useful in many cases (see, for example, *Valentine* [1987]) but can be dangerous if care is not used, because it relies on an analogy between turbulent transport and molecular transport as determined by kinetic theory (see discussions by *Tennekes and Lumley* [1972, pp. 8–14, 57]). In light of this analogy, we have chosen only to model what we feel is a reasonable minimum turbulence viscosity so that

$$\nu = 0.2L|\mathbf{u}| \quad (5)$$

where the length scale L is set at 100 m, the mesh size in our numerical solutions. Equation (5) is appropriate for a mean eddy diameter in the turbulent flow of about 20 m, a conservative approximation based on the scale of turbulence eddies observed in historic Plinian eruptions (ranging up to several hundred meters in diameter). Again, we emphasize that this treatment of turbulence viscosity is not intended to be physically rigorous but only to give a crude minimum approximation of turbulence effects.

When (1)–(3) are written in expanded form for cylindrical coordinates in two dimensions, the result is a system of eight coupled, nonlinear, partial differential equations with 16 dependent variables. Closure of the partial differential equations is obtained by applying the following algebraic relationships (equations (6)–(12)):

$$I_s = c_{vs}T_s \quad (6a)$$

$$I_g = c_{vg}T_g \quad (6b)$$

$$p = (\gamma - 1)\rho_g I_g \quad (7)$$

$$\theta_g = 1 - \theta_s \quad (8)$$

$$K_g = -K_s \quad (9)$$

$$R_g = -R_s \quad (10)$$

TABLE 1. Material Properties and Values of Physical Parameters Used in Numerical Experiments

Parameter	Value	Reference
a_g	0.9	*Flaud et al.* [1977]
c_d	1.0	*Walker et al.* [1971]
c_{vg}	1406 J/kg K	*Reynolds and Perkins* [1977, p. 642]
c_{vs}	954 J/kg K	*Riehle* [1973]
c_{pg}	1867 J/kg K	*Reynolds and Perkins* [1977, p. 642]
e_s	0.8	*Weast* [1979, p. E393]
g	9.8 m/s^2	
k_g	0.5 W/m K	*Incropera and DeWitt* [1981, p. 779]
ε	5.670×10^{-8} W/m^2 K^4	
γ	1.33	*Reynolds and Perkins* [1977, p. 642]
ν_g*	1.1×10^{-4} m^2/s	*Incropera and DeWitt* [1981, p. 779]
ρ_s†	2400 kg/m^3	

*This value of ν_g is used in equations (12)–(14), the heat exchange terms, and in the appendix.
†In runs 50–52, ρ_s = 500 kg/m^3 (pumice).

Equations (6*a*) and (6*b*) are the thermal equations of state for each phase, with c_{vs} and c_{vg} being the specific heats at constant volume for the solid and gas phases, respectively. Specific heats are treated as constants (for values, see Table 1). Equation (7) is the mechanical equation of state for the gas phase, with γ, a constant, being the ratio of specific heats at constant pressure and constant volume of the gas. Equation (8) relates the volume fraction of the gas phase to that of the solid phase. Equations (9) and (10) state that momentum and heat transfer between phases are coupled in such a manner that a gain in momentum/heat by one phase is the result of loss or momentum/heat in the other phase.

The functions K_s and R_s are given by

$$K_s = \frac{3\theta_s\rho_g c_d}{16 r_s}\,|\mathbf{u}| \tag{11}$$

$$R_s = \frac{-3\theta_s\varepsilon}{r_s}\,[e_s T_s^4 - a_g T_g^4] - \frac{3\theta_s k_g}{2r_s^2}\,[2.0 + 0.6(Ry_s^{1/2} Pr_g^{1/3})\,\Delta T \tag{12}$$

where

$$Ry_s = \frac{2r_s|\Delta\mathbf{u}|}{\nu_g} \tag{13}$$

$$Pr_g = \frac{c_{pg}\rho_g\nu_g}{k_g} \tag{14}$$

$$\Delta T = T_s - T_g \tag{15}$$

Equation (11) is simplified from *Harlow and Amsden* [1975] in which c_d is a drag coefficient (taken as unity for this work following the analysis of *Walker et al.* [1971]) and r_s is the radius of the particles. Equation (12), the heat transfer function, is the sum of heat transfer due to radiation and forced convection. In the radiative heat transfer term, ε is the Stefan-Boltzmann constant, and a_g and e_s are the absorptivity of the gas and emissivity of the particles, respectively (note that this is written to represent radiative transport from the particles to the gas). For conditions of interest here, particles emit radiation in the near-infrared region of the electromagnetic spectrum, so that the gas phase (water vapor) has $a_g \simeq 0.9$ [*Flaud et al.*, 1977] and the particle phase has $e_s \simeq 0.8$. The forced-convection term in (12) is an empirical relation involving Reynolds and Prandtl numbers (equations (13) and (14)), with $c_{pg} = \gamma c_{vg}$ and ν_g being the kinematic viscosity of the gas alone (Table 1). Detailed discussions and development of the terms in (12) for single spheres are given by *Bird et al.* [1960, chapters 3 and 4] (note that (12) accounts for more than one particle, as determined by θ_s and r_s). Radiative heat transfer is minor compared to heat transfer via forced convection for cases of interest here.

The computational domain is shown in Figure 1. The axis of the flow is modeled as a rigid reflector in order to preserve the symmetry of the system. The Earth's surface is modeled as a smooth, free-slip reflector because any boundary layer phenomena are expected to occur on a scale too small to be resolved by the mesh. The upper and right-hand edges of the domain are "open" to allow flow out of the domain. The atmosphere is gravitationally stable with an exponential density stratification and is modeled as a perfect gas with the same isentropic exponent as the erupting gas ($\gamma = 1.33$), a value similar to atmospheric air which has $\gamma = 1.4$. This simplification greatly reduces the required computation time; inclusion of air in the calculations would involve adding another set of conservation equations with attendant coupling expressions. The computational domain covers an area of 7 × 7 km and is divided into an Eulerian (fixed reference frame) grid of 100 × 100 m squares. The time step for computation is set at 0.02 s, which satisfies the Courant condition for flow speeds up to 5000 m/s. Eruption discharge begins at $t = 0$ and computation of the flow field continues until $t = 200$ s, which roughly corresponds to the achievement of steady state flow within the computational domain for most runs. Eruption discharge rate is fixed for these steady discharge experiments, in contrast to earlier simulations carried out by *Wohletz et al.* [1984], where discharge was a time-dependent, computed condition because of nonsteady flow. All of the numerical experiments reported here have exit temperatures of 1200 K. The computer code, "DASH" (dusty air shock), originally written by T. Cook and F. Harlow of Los Alamos National Laboratory, has been modified for applications to volcanic problems by *Horn* [1986].

Fifty-one numerical experiments were completed in order to make a sensitivity study of the effect of various initial and boundary conditions upon the modeled eruption. Of greatest interest were the effects of differing values of inflow gas pressure, velocity, particle loading, and particle size at the vent

TABLE 2. Exit Conditions of Model Eruptions

Run	v_e, m/s	θ_s	P_e, MPa	R_v, m	r, m	D, kg/s	Tg_m	Ri_m	Pn	K_p	Ds	M	PL/F*	t_D,† s
8	300	10^{-2}	0.1	200	10^{-4}	1.8×10^9	0	47.3	2.8×10^{-2}	1.0	33.4	4.7	F	200
10	200	10^{-2}	0.1	200	10^{-4}	6.0×10^8	0	21.0	4.2×10^{-2}	1.0	33.4	3.1	F	200
11	100	10^{-2}	0.1	200	10^{-4}	3.0×10^8	0	5.3	8.4×10^{-2}	1.0	33.4	1.6	F	200
12	200	10^{-2}	0.1	200	10^{-4}	6.0×10^8	0	21.0	4.2×10^{-2}	1.0	33.4	3.1	F	40
13	200	10^{-2}	0.1	200	10^{-4}	6.0×10^8	0	21.0	4.2×10^{-2}	1.0	33.4	3.1	F	25
14	200	10^{-2}	0.1	200	10^{-4}	6.0×10^8	0	21.0	4.2×10^{-2}	1.0	33.4	3.1	F	15
15	200	10^{-2}	0.1	200	10^{-4}	6.0×10^8	0	21.0	4.2×10^{-2}	1.0	33.4	3.1	F	60
16	150	10^{-2}	0.1	200	10^{-4}	4.5×10^8	0	11.8	5.6×10^{-2}	1.0	33.4	2.3	F	200
17	250	10^{-2}	0.1	200	10^{-4}	7.5×10^8	0	32.9	3.3×10^{-2}	1.0	33.4	3.9	F	200
18	200	10^{-2}	0.1	200	10^{-4}	6.0×10^8	0	21.0	4.2×10^{-2}	1.0	33.4	3.1	F	5
19	200	10^{-2}	0.1	200	10^{-4}	6.0×10^8	0	21.0	4.2×10^{-2}	1.0	33.4	3.1	F	50
21‡	300	10^{-2}	0.01	200	10^{-4}	1.8×10^9	−2.0	47.3	8.8×10^{-2}	0.1	33.4	14.8	F	200
22	300	10^{-2}	1.0	200	10^{-4}	9.7×10^8	18.3	42.2	8.8×10^{-3}	10.0	35.9	1.5	PL	200
23	200	10^{-2}	0.5	200	10^{-4}	6.2×10^8	8.5	21.0	1.9×10^{-2}	5.0	34.6	1.4	F	200
24§	200	10^{-2}	1.0	200	10^{-4}	6.5×10^8	18.3	21.0	1.3×10^{-2}	10.0	35.9	1.0	F	200
25§	200	10^{-2}	1.5	200	10^{-4}	6.7×10^8	27.5	21.0	1.1×10^{-2}	15.0	37.1	0.8	PL	200
26§	200	10^{-2}	2.0	200	10^{-4}	6.9×10^8	36.2	21.0	9.3×10^{-3}	20.0	38.3	0.7	PL	200
31‡	200	5×10^{-2}	0.1	200	10^{-4}	3.0×10^9	0	20.5	4.2×10^{-2}	1.0	167.3	7.1	F	200
32‡	200	10^{-1}	0.1	200	10^{-4}	6.0×10^9	0	20.5	4.2×10^{-2}	1.0	334.3	10.3	F	200
33	200	5×10^{-3}	0.1	200	10^{-4}	3.0×10^8	0	21.7	4.2×10^{-2}	1.0	17.0	2.2	F	200
34	100	10^{-2}	0.1	300	10^{-4}	6.8×10^8	0	3.5	8.4×10^{-2}	1.0	33.4	1.6	F	200
35	200	10^{-2}	0.1	300	10^{-4}	1.4×10^9	0	14.0	4.2×10^{-2}	1.0	33.4	3.1	F	200
36	300	10^{-2}	0.1	300	10^{-4}	2.0×10^9	0	31.5	2.8×10^{-2}	1.0	33.4	4.7	F	200
38	100	10^{-2}	0.1	200	10^{-2}	3.0×10^8	0	5.3	8.4×10^{-1}	1.0	33.4	···	F	200
39	200	10^{-2}	0.1	200	10^{-2}	6.0×10^8	0	21.0	4.2×10^{-1}	1.0	33.4	···	F	200
40	300	10^{-2}	0.1	200	10^{-2}	1.8×10^9	0	47.3	2.8×10^{-1}	1.0	33.4	···	F	200
41	100	10^{-2}	0.1	200	10^{-1}	3.0×10^8	0	5.3	2.6×10^{0}	1.0	33.4	···	F	200
42	200	10^{-2}	0.1	200	10^{-1}	6.0×10^8	0	21.0	1.3×10^{0}	1.0	33.4	···	F	200
43	300	10^{-2}	0.1	200	10^{-1}	1.8×10^9	0	47.3	8.8×10^{-1}	1.0	33.4	···	F	200
46	300	10^{-2}	0.1	200	10^{-3}	1.8×10^9	0	47.3	8.8×10^{-2}	1.0	33.4	···	F	200
47	100	10^{-2}	0.1	200	10^{-3}	3.0×10^8	0	5.3	2.6×10^{-1}	1.0	33.4	···	F	200
49	300	10^{-2}	0.69	200	10^{-4}	1.8×10^9	12.3	47.3	1.1×10^{-2}	6.9	33.7	1.8	PL	200
50¶	300	10^{-2}	0.1	200	10^{-2}	1.9×10^8	0	53.3	1.3×10^{-1}	1.0	7.2	···	F	200
51¶	300	10^{-2}	0.1	200	10^{-1}	1.9×10^8	0	53.3	4.0×10^{1}	1.0	7.2	···	F	200
52¶	300	10^{-2}	0.1	200	10^{-3}	1.9×10^8	0	53.3	4.0×10^{-2}	1.0	7.2	···	F	200
53	300	10^{-2}	0.37	200	10^{-4}	1.0×10^9	5.7	47.3	1.4×10^{-2}	3.7	36.8	2.4	F	200
54§	100	10^{-2}	1.38	300	10^{-4}	7.5×10^8	16.9	3.5	2.2×10^{-2}	13.8	36.8	0.4	F	300
55§	100	10^{-2}	2.06	300	10^{-4}	7.8×10^8	24.7	3.5	1.8×10^{-2}	20.6	38.5	0.3	PL	200
56	300	10^{-2}	1.03	300	10^{-4}	2.2×10^9	12.6	31.5	8.7×10^{-3}	10.3	36.0	1.5	PL	200
57§	300	10^{-2}	1.38	300	10^{-4}	2.2×10^9	16.9	31.5	7.5×10^{-3}	13.8	36.8	1.2	PL	200
58§	300	10^{-2}	1.38	300	10^{-1}	2.2×10^9	16.9	31.5	2.4×10^{-1}	13.8	36.8	···	F	200
59	300	10^{-2}	0.69	300	10^{-1}	2.1×10^9	8.5	31.5	3.4×10^{-1}	6.9	33.7	···	F	200
60	205	3.1×10^{-3}	0.1	100	10^{-4}	4.8×10^7	0	47.3	4.1×10^{-2}	1.0	10.5	1.7	F	200
61§	73	1.3×10^{-3}	0.1	200	10^{-4}	3.0×10^7	0	3.5	1.1×10^{-1}	1.0	4.5	0.4	F	200
62	226	1.6×10^{-3}	0.1	200	10^{-4}	1.2×10^8	0	31.5	3.7×10^{-2}	1.0	5.7	1.4	F	200
63	312	2.6×10^{-2}	1.0	200	10^{-4}	2.5×10^9	7.2	50.2	8.5×10^{-3}	10.0	89.7	2.5	F	200
64	244	7.0×10^{-3}	0.5	200	10^{-4}	5.4×10^8	12.0	31.5	1.5×10^{-2}	5.0	24.6	1.4	F	200
65	202	2.0×10^{-2}	1.0	200	10^{-4}	1.2×10^9	9.5	21.0	1.3×10^{-2}	10.0	68.6	1.4	F	200
66§	171	9.5×10^{-4}	0.1	100	10^{-4}	1.3×10^7	0	21.0	4.9×10^{-2}	1.0	3.4	0.8	F	200
67§	128	1.1×10^{-3}	0.2	100	10^{-4}	1.4×10^7	36.2	21.0	4.6×10^{-2}	2.0	4.9	0.5	F	200
68§	131	1.7×10^{-3}	0.2	100	10^{-4}	1.8×10^7	27.5	21.0	4.5×10^{-2}	2.0	6.2	0.6	F	200
69	374	2.1×10^{-2}	1.0	300	10^{-4}	5.6×10^9	5.7	47.3	7.1×10^{-3}	10.0	73.8	2.7	PL	200

*PL, Plinian column; F, fountain (collapsing column).
†t_D is duration of discharge.
‡Designates runs where v_e is larger than twice the value predicted by approach of *Wilson et al.* [1980].
§Designates runs where v_e is less than half the value predicted by approach of *Wilson et al.* [1980].
¶In these runs, ρ_s = 500 kg/m^3 (similar to pumice). In all other runs, ρ_s = 2400 kg/m^3.

exit plane. Table 2 lists these conditions for all the computer runs, and particular models will be identified by their run number. Because the solutions obtained are listed by the computer for each variable given above and for each computational cell and time step, a large volume of numerical results was generated. Each run produced more than 5000 pages of printed data. Graphics programs were written to produce six r-z contour plots of θ_s, log θ_s, ρ_g, p, T_s, and T_g for specified time steps. Two additional r-z vector plots show $\mathbf{u}_s$ and $\mathbf{u}_g$. More than 400 plots were recorded for each run. Each run required about 2.5 hours of Cray-1 time (note that this machine vectorizes arrays and operates at a rate of about 10^8 floating point operations per second). By analogy, one can say that analysis of the large volume of numerical data produced by each run is similar to conducting a field study of pyroclastic deposits in which one would like to sample particle sizes, textures, and compositions at several hundred points in each stratigraphic unit.

A brief explanation of our choices of vent-exit parameters is appropriate. We chose parameter values that would cover a reasonable range of conditions for explosive eruptions. In our models, individual parameters were specified independently, although in reality all of the variables are related to each other and depend upon the flow within the volcanic conduit. For example, *Wilson et al.* [1980] calculate the range of possible exit conditions based upon a single-phase, one-dimensional flow approximation. In their calculations the conduit geometry is fixed and pressures within the conduit are assumed to equal lithostatic pressure. L. Wilson (personal communication, 1988) has compared our model exit parameters (Table 2) with predictions based upon the model of *Wilson et al.* [1980] and has pointed out that a large number of our experiments are not consistent with the *Wilson et al.* [1980] model. While we acknowledge the importance of the *Wilson et al.* [1980] calculations as setting a framework for flow within volcanic conduits and are aware that our exit parameters are not all consistent with their calculations, we feel that the actual range of exit parameters that may occur in nature is too poorly known at this time to put detailed constraints on exit parameters. This is due to four main aspects that have not been addressed in previous models: (1) nonlinear, time-dependent interaction between the flows and the conduit geometry (e.g., erosion, wall bursting), (2) multiphase effects, (3) two- and three-dimensional effects, and (4) the possibility of nonlithostatic pressure in the flow. We are currently pursuing modeling that will at least partially account for these effects in order to learn more about the range of possible exit conditions. We point out that all but a few of the experiments discussed in this paper are within a factor of 2 of parameter values allowed by the *Wilson et al.* [1980] model. Considering the difference in the approaches to the problem, this factor is not unreasonable. Experiments which vary by a factor larger than 2 (in terms of exit velocities predicted by the Wilson et al. model) are noted in Table 2. The largest deviation from *Wilson et al.* [1980] predictions is by a factor of 8.

Dimensionless Parameters

The proper approach for study of the large volume of numerical data is to nondimensionalize parameters in order to find systematic trends. The dimensional analysis given here arises from the momentum equations (2*a*) and (2*b*) as defined by exit conditions and as such lends insight into the interplay of forces acting on an eruption column as it exits the vent.

We focus on those variables that affect the large-scale behavior of eruption columns. Examination of the momentum equations (2*a*) and (2*b*) reveals four different types of forces: (1) inertia, (2) pressure gradient, (3) interphase drag, and (4) gravitation. Forces involving molecular or "dusty gas" viscosity are negligible compared to these forces, as shown in the appendix, and the effects of the turbulence viscosity are not considered in this discussion. The pressure gradient at the vent can be represented by the difference between exit pressure and local atmospheric pressure. Interphase drag or momentum coupling can be represented by the settling velocity of particles, with low settling velocities reflecting good coupling. Gravitational forces acting on an eruption column are determined by the density difference between the erupting mixture and the ambient atmosphere and the size scale of the column which is measured by the vent radius. Gravitational forces thus can be also called buoyancy forces, since an eruption column exiting with a bulk density equal to that of the atmosphere will experience no downward acceleration from gravity.

All these effects are put into ratios to form the following parameters:

$$Tg_m = \frac{p_e - p_{\text{atm}}}{(\rho_m - \rho_{\text{atm}})gR_v} \tag{16}$$

$$Pn = \frac{w_s}{v_e} \tag{17}$$

$$Ri_m = \frac{\rho_m v_e^{\,2}}{(\rho_m - \rho_{\text{atm}})gR_v} \tag{18}$$

For these equations, subscript e refers to conditions at the vent exit plane, v_e being the initial vertical velocity (both phases are assigned equal velocities at the exit) and w_s being the terminal velocity of the particles. Setting velocity is arrived at by balancing gravitational and drag forces on a particle so that, within the simplified treatment in this paper,

$$w_s = \left[\frac{16 r_s g(\rho_s - \rho_g)}{3 c_d \rho_g}\right]^{1/2} \tag{19}$$

The mixture density is determined by $\rho_m = \theta_s\rho_s + \theta_g\rho_g$. R_v is the vent radius. In words, Tg_m, here referred to as the "thermogravitational parameter," is a ratio of thermodynamic (pressure) driving forces to buoyancy forces; Pn, the Rouse number, is a ratio of clast settling velocity to upward flow velocity; and the Richardson number, Ri_m, is a ratio of inertial forces to buoyancy forces. The subscript m indicates that these parameters are defined in terms of the properties of the erupting mixture. For very small particles with low values of the Rouse number the mixture will behave nearly as a single continuum, since the particles are in near-equilibrium with the gas both thermally and dynamically.

Another parameter that affects the large-scale dynamics of the eruption column is the ratio of exit pressure to ambient pressure, K_p, given by

$$K_p = p_e/p_{\text{atm}} \tag{20}$$

This parameter influences the shape and velocity field of the column [*Liepmann and Roshko*, 1957; *Kieffer*, 1984] and is discussed in detail in a forthcoming section. Other parameters that will be discussed in this paper include the density ratio (Ds) defined by

$$Ds = \rho_m/\rho_{\text{atm}} \tag{21}$$

and the Mach number M defined by

$$M = u_m/c_m \tag{22}$$

where the mixture sound speed c_m is given by [*Kieffer*, 1981]

$$c_m = \left[\frac{(c_{pg} + mc_{vs})}{(c_{vg} + mc_{vs})}\frac{c_{vg}(\gamma - 1)T}{(1 + m)}\right]^{1/2} \tag{23}$$

In this equation, m is the mass ratio of solids to gas and $c_{vg}(\gamma - 1) = c_{pg} - c_{vg}$ equals the gas constant for steam. The Mach number as defined here only holds for small particles with low Pn, so that the mixture can be approximated as a single continuum (pseudodgas). Note that u_m in (22) is the magnitude of the velocity of the mixture, implying that there is no slip between phases. For runs where particles are larger than 10^{-4} m, M is not calculated because the mixture velocity and sound speed are both poorly defined.

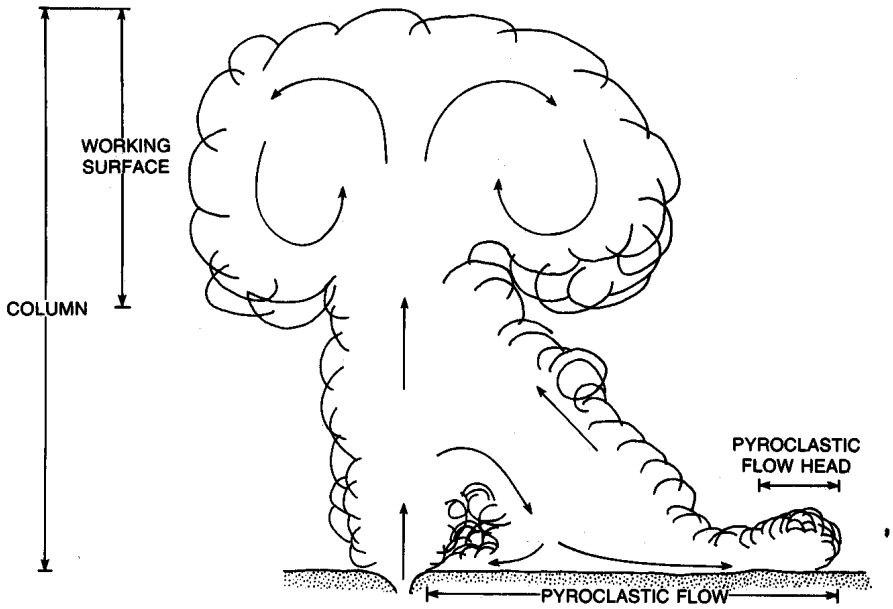

Fig. 2. Illustration of terminology for various features of a Plinian eruption.

Dimensional and dimensionless parameters for all runs reported in this paper are tabulated in Table 2. Included in Table 2 are values of mass discharge rate of magma ($D = \pi R_v^2 \rho_m v_e$) for comparison with previously published values.

General Features of the Numerical Experiments

Terms used in this paper are illustrated in Figure 2. The "column" designates the main vertical part of the eruption flow field above the vent. The "working surface" is at the top of the column, where large-scale vorticity and an increased diameter result from the column's penetration into the atmosphere. This term is adapted from *Blandford and Rees* [1974] and *Norman et al.* [1982], who have modeled the structure of high-speed jets for astrophysical applications. When a column does not collapse, it will be referred to as a "Plinian column"; if it does collapse, it will be referred to as a "fountain." The laterally moving, ground-hugging flow that results from a fountain is called a "pyroclastic flow." The word "flow" will be used to describe fluid motions in general unless it is preceded by "pyroclastic," which restricts it to the above definition. "Pyroclastic flow head" is the front of a pyroclastic flow.

Two example numerical experiments are shown in Figures 3 and 4. The plots show several types of information. Contours of the logarithm of ash volume fraction (θ_s), each contour being an order of magnitude different from neighboring contours, give an idea of the morphology of the cloud and the distribution of particles. The innermost contour, where most of the ash in a given eruption resides, corresponds to particle volume fraction one order of magnitude less than θ_s at the exit plane. The velocity field of the solid phase, $\mathbf{u}_s$, is superimposed on the volume-fraction plots (these plots are referred to as θ-$\mathbf{u}_s$ plots). Velocity vectors are drawn outward from the center of each computational cell in the direction of flow and with length proportional to flow speed. The combined θ_s-velocity plots are especially useful because they give information about the shape and motion of the eruption cloud, which can be compared to observed natural eruptions. Pressure and density contours are shown for the compressible (gas) phase, and temperature contours of the solid phase are also given. Plots of gas temperature and velocity are not shown here but are very similar to the corresponding ones for the solid field.

The eruption discharge begins at time zero. The fast flow of dense material into the atmosphere results in an initial compression pulse that travels away from the vent as a hemispherical wave. Gas density and pressure plots at early times display this pulse. In this numerical model the pressure signal is diffused over several computational cells, but in nature it is likely that this signal would form a shock (pressure discontinuity) after traveling a small distance from the vent [*Wohletz et al.*, 1984]. As eruption time progresses, the eruption columns continue to rise, and at late time, the models shown in Figures 3 and 4 begin to differ significantly in their behavior. For the conditions shown in Figure 3 the eruption column begins to spread laterally at several kilometers altitude, but after the spreading, it continues to rise until the working surface is out of the computational domain. For the conditions of Figure 4 the column also begins to spread laterally at several kilometers altitude, but instead of continuing upward, the part of the column that has spread then falls back to the ground, resulting in a pyroclastic flow. The interpretation of these two types of behavior follows volcanologic observation: Figure 3 represents an eruption that produces a high-standing Plinian column, while Figure 4 is a fountain that produces pyroclastic flows. Details of the behavior of noncollapsing and collapsing columns are discussed below, but first we quantify the conditions that determine whether or not a column will collapse.

Eruption Column Collapse

As discussed in the section on dimensionless parameters, the variables affecting the large-scale behavior of eruption columns are summarized in the parameters Tg_m, Ri_m, Pn, and K_p. Special attention is given here to Tg_m, Ri_m, and K_p. The effect of the Rouse number Pn is such that a column containing large-Pn clasts will tend to collapse under conditions that would otherwise produce a Plinian column. This result illustrates the tendency of coarse, dense clasts to follow nearly ballistic paths. We emphasize that in DASH we consider only one particle size per run and therefore can not reproduce size

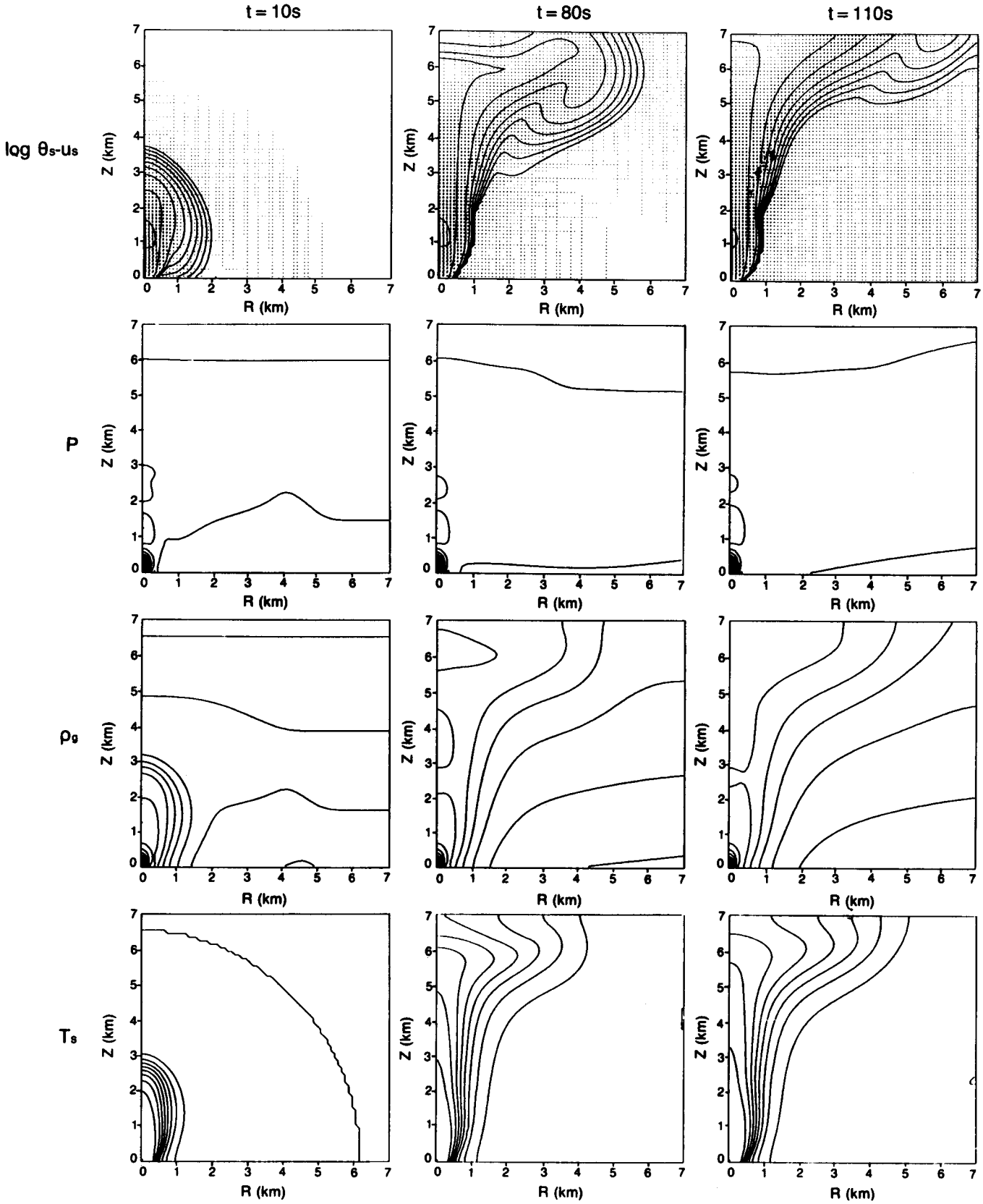

Fig. 3. Numerical eruption producing a Plinian column (run 49). Contour plots of log θ_s-$\mathbf{u}_s$, p, ρ_g, and T_s are shown for three times after initiation of discharge (10, 80, and 110 s). The innermost log θ_s contour corresponds to $\theta_s = 10^{-3}$, and each contour outward represents an order of magnitude decrease in θ_s. Maximum flow speeds of about 400 m/s are attained in the basal 2 km of the column. The exit pressure of this eruption is 0.69 MPa ($K_p = 6.9$). The initial atmospheric pressure signal is shown in the pressure and gas-density plots at $t = 10$ s as a perturbation in the ambient values. T_s contours are drawn at 100 K intervals, starting at 1200 K at the vent, so that the outermost temperature contour corresponds to 400 K. See detail of the basal portion of the column in Figure 6.

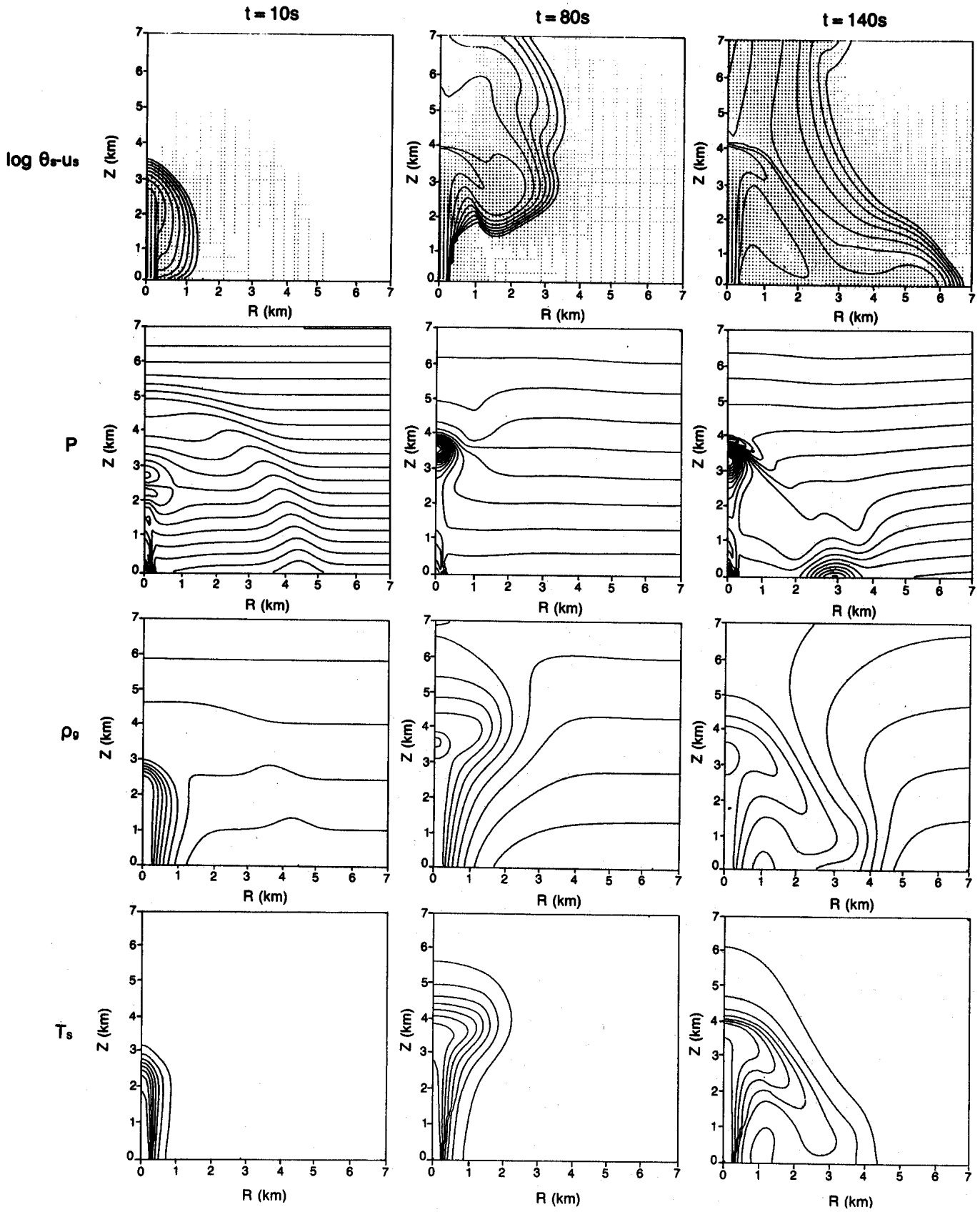

Fig. 4. Numerical experiment producing a pyroclastic fountain (run 8). Contour plots of log θ_s-$\mathbf{u}_s$, p, ρ_g, and T_s are shown at $t = 10$, 80, and 140 s. The innermost θ_s contour corresponds to a solid volume fraction of 10^{-3}, and maximum speed of 300 m/s occurs at the exit plane. The exit pressure of this eruption equals the ambient pressure ($K_p = 1$). Note the atmospheric pressure signal at $t = 10$ s, which shows with better resolution than the eruption of Figure 3 because pressure contours are drawn at smaller intervals for this run. High-pressure cells are located at the elevation of collapse and where the collapsing flow impinges upon the ground. The contour plot of ρ_g at $t = 140$ s shows how hot, relatively low-density gas is dragged beneath relatively high-density ambient gas by the solid phase, producing an unstable situation where the hot gas tends to rise out of the basal flow. This in turn leads to development of a cloud of ash that rises above the basal pyroclastic flow due to buoyancy. T_s contours follow closely the plot of ρ_g.

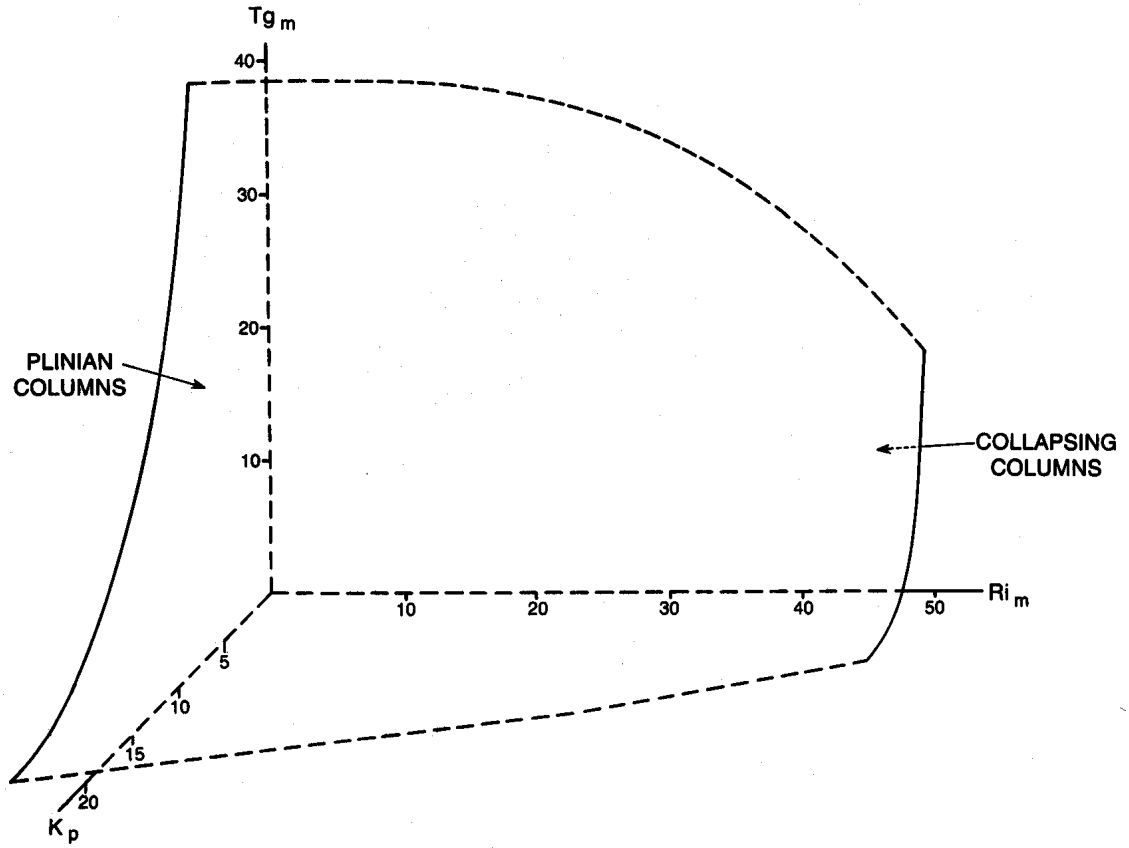

Fig. 5. Collapse of eruption columns (assuming similar particle size characteristics) is determined largely by the values of Tg_m, Ri_m, and K_p as defined for exit conditions. Critical conditions for column collapse appear to form a surface in three-dimensional space defined by these three parameters, as shown here. Exit conditions that plot above the surface produce Plinian columns, while those below the surface produce collapsing columns or fountains leading to pyroclastic flows.

distributions that are found in nature; this restriction limits the full interpretation of particle size effects. So, while it is reasonable to predict that an overall increase in *Pn* will produce a tendency toward column collapse, we do not seek to quantify this relationship within the context of our single-particle-size model. On the other hand, by varying the properties of the eruptive mixtures, while retaining a constant particle size (approximately constant *Pn*), we can compare the behavior of the eruptions with constant size distributions.

Intuitively, one might expect a large Tg_m to be typical of Plinian columns, since this implies a large upward driving force from the pressure gradient relative to the downward force of negative buoyancy (where the column exits with a density larger than that of the atmosphere). The same is true of the Richardson number: a large initial component of inertia will counteract the negative buoyancy. Indeed, the Richardson number, which is determined by the mixture density (directly related to exsolved gas content), exit velocity, and vent radius, embodies all the variables considered by *Sparks et al.* [1978], *Wilson et al.* [1980], and *Wilson and Walker* [1987]. Since Tg_m and Ri_m contain all the major forces acting on an eruption column, a collapse criterion might be completely defined in terms of these two parameters. In the course of the numerical experiments, however, it was found that column collapse is also very sensitive to the pressure ratio. This result follows from the effect of overpressure ($Kp > 1$) on column structure [*Kieffer*, 1981, 1982, 1984; *Kieffer and Sturtevant*, 1984]: as supersonic flow exits a vent, the gas phase expands and accelerates to achieve pressure equilibrium with the atmosphere. This gas expansion decreases the flow's bulk density and thus decreases the magnitude of the negative buoyancy force (details of jet structure in the model runs will be discussed in a later section). The transfer of kinetic energy to internal energy that takes place across the subsequent shock (referred to as the Mach disk shock) is mainly reflected in a temperature increase and velocity decrease. Above the Mach disk shock, velocity returns to values very similar to those found at equivalent altitudes in a pressure-balanced jet. However, the mixture density does not increase very much across the shock so that there is a net decrease of density relative to a pressure-balanced jet. Thus, after going through the initial expansion and shock stage the flow still has a large velocity, but the negative buoyancy force is greatly reduced. The importance of the pressure ratio relative to the density ratio is shown in several of the numerical experiments. For example, run 26 ($K_p = 20$) has an exit density about nine times as large as run 67 ($K_p = 2$). Even though they have the same values of Tg_m and Ri_m, the denser run forms a Plinian column, and the less dense run forms a fountain simply because of the strong effect of supersonic gas expansion.

In summary, three dimensionless parameters (Tg_m, Ri_m, and K_p) can be used to determine the conditions necessary for Plinian columns or fountains. A column collapse criterion, established by a sensitivity analysis of the computer results, forms a surface in Tg_m-Ri_m-K_p space (Figure 5). Although this criterion does not directly apply to natural eruptions because of the simplifications inherent in the model, it does demonstrate how the main driving forces combine in a nonlinear

(and not necessarily intuitive) manner to control the dynamics of an eruption column. In terms of measurable eruption quantities this criterion suggests that, in general, if conditions in an eruption tend toward lower exit pressure, lower exit velocity, higher mixture density (lower gas content), and larger vent radius, then that eruption will tend to evolve toward a collapsing column or fountain. Values of the dimensionless parameters are coupled (e.g., pressure is affected by vent radius), so the parameters cannot be considered independent of each other.

Sparks et al. [1978], *Wilson et al.* [1980], and *Wilson and Walker* [1987] proposed collapse criteria based upon the effects of exit velocity, gas content, and vent radius. The important difference between results presented here and the previous criteria is the inclusion of thermodynamic (pressure) effects. The previous criteria, as mentioned earlier, do not directly account for the thermodynamics of the flows because they assume that columns are pressure-balanced and remain in equilibrium with the local ambient pressure at all heights above the vent. Since pressure fluctuations of at least a few bars are to be expected during an eruption (even during the steady phases of discharge, because of vent erosion), it is of primary importance to account for exit pressure. Formation of a Plinian column does not depend only upon entrainment and heating of atmospheric air. Although it is clear from observations that turbulence and related entrainment operate to some degree during Plinian eruptions, the pressure effects presented here do not support the earlier assumption that column behavior is determined entirely by the efficiency of air entrainment.

Evolution of the Modeled Eruption Columns

Noncollapsing column (Plinian). We now focus on the model eruption shown in Figure 3 (run 49). The various plots are shown for times of 10, 80, and 110 s after discharge begins. Conditions for this eruption (Table 2) place it above the surface separating Plinian columns from fountains in Figure 5. The eruption is overpressured, which plays an important role in its appearance and behavior.

By $t = 10$ s the top of the column is at about 3.5 km elevation (Figure 3). Velocity vectors within the plume show an initial radial-outward flow immediately above the vent followed by a radial-inward flow above about 1.5 km elevation. Between about 0.8 and 1.5 km there is a region of low θ_s directly corresponding to a region of low pressure. These features are related to the internal structure of the supersonic, overpressured column. The velocity vectors show vortex development at just above 2 km elevation (not visible in Figure 3); this structure corresponds to the rolling vortex of the working surface that is observed in natural eruptions and laboratory experiments [*Kieffer and Sturtevant*, 1984]. Overall, the eruption column at this stage is rather wide due to initial radial flow. The atmospheric pressure signal, apparent in the gas pressure and density plots, has reached a distance of about 5 km from the vent, and about 4 s later it propagates out of the computational domain.

Plots for $t = 80$ s show the outer sheath of the column continuing to be pulled upward into the rolling vortex, which has experienced an outward displacement in addition to its general upward movement. The lower 1 km of the column shows the characteristic flaring or diamondlike structure of overpressured jets (the steplike appearance of this flaring is an artifact of the numerical mesh). Regions of relative low and high gas pressure and density further illustrate the typical structure of an overpressured jet. Near the top of the computational domain the gas pressure within the column is somewhat higher than that of the adjacent atmosphere. This is due to a decrease in velocity at this elevation and resultant conversion of kinetic energy to internal energy. By $t = 110$ s the velocity at this elevation has increased, and pressure has decreased accordingly. Also at $t = 110$ s the rolling vortex, which has spread laterally to the edge of the computational domain, is beginning to accelerate rapidly upward and out of the domain, and by $t = 140$ s (not shown) the working surface has completely exited the computational domain.

As mentioned earlier, the external form displayed by the model column reflects the internal structures typical of overpressured jets, and it is appropriate at this point to discuss in some detail the internal structure of the overpressured run 49. In particular, we focus on the lowest 2.5 km, where jet dynamics as discussed by *Kieffer* [1981, 1984] and *Kieffer and Sturtevant* [1984] dominate the flow. Figure 6 shows detailed radial profiles of pressure, solid volume fraction, and mixture density at 500-m intervals above the vent when $t = 64$ s. At each elevation interval, local atmospheric pressure and density are shown by dashed lines. The outer edge of the eruption column corresponds to the location of the $\theta_s = 10^{-6}$ contour, which approximates the visible edge of the eruption column [*Horn*, 1986].

At zero elevation (the exit plane) the pressure exceeds atmospheric (by a factor of 6.9 in this case) in the inner 200 m. Although the vent has a radius of 200 m, the mixture immediately expands to give the column a basal radius of slightly more than 400 m. Beyond the edge of the vent, however, the flow has undergone Prandtl-Meyer expansion to a pressure slightly lower than atmospheric. Because of this expansion of the gas phase, θ_s is decreased by more than an order of magnitude relative to its exit value. Mixture density follows the trend of solid volume fraction.

At 500 m the amount of overpressure in the core of the column has decreased significantly compared to conditions at the vent. Along the margins of the column, beyond about 300 m from its center, the pressure has increased relative to the zero elevation value, so that it is nearly equal to the local atmospheric pressure. The θ_s and mixture density have maximum values at the center of the column and decrease outward.

At 1000 m elevation the pressure within the inner 500 m of the column is substantially lower than local atmospheric pressure. Beyond this inner region, the flow is close to atmospheric pressure. This distribution of pressure is the result of overcompensation of the flow in its trend toward pressure equilibrium with the atmosphere and produces θ_s and mixture density profiles with maxima located away from the center of the column. At 1500 m elevation the pressure within the inner 300 m of the column is still less than atmospheric, and the outer part of the column is now slightly overpressured relative to the atmosphere. Again, the solid-volume-fraction and mixture-density plots have maxima located away from the center of the flow.

By 2000 m elevation the core of the flow has recompressed so that it has a pressure slightly higher than the local atmospheric; θ_s and ρ_{mix} have maximum values in the center of the column and decrease steadily outward.

These phenomena can be explained in terms of observations

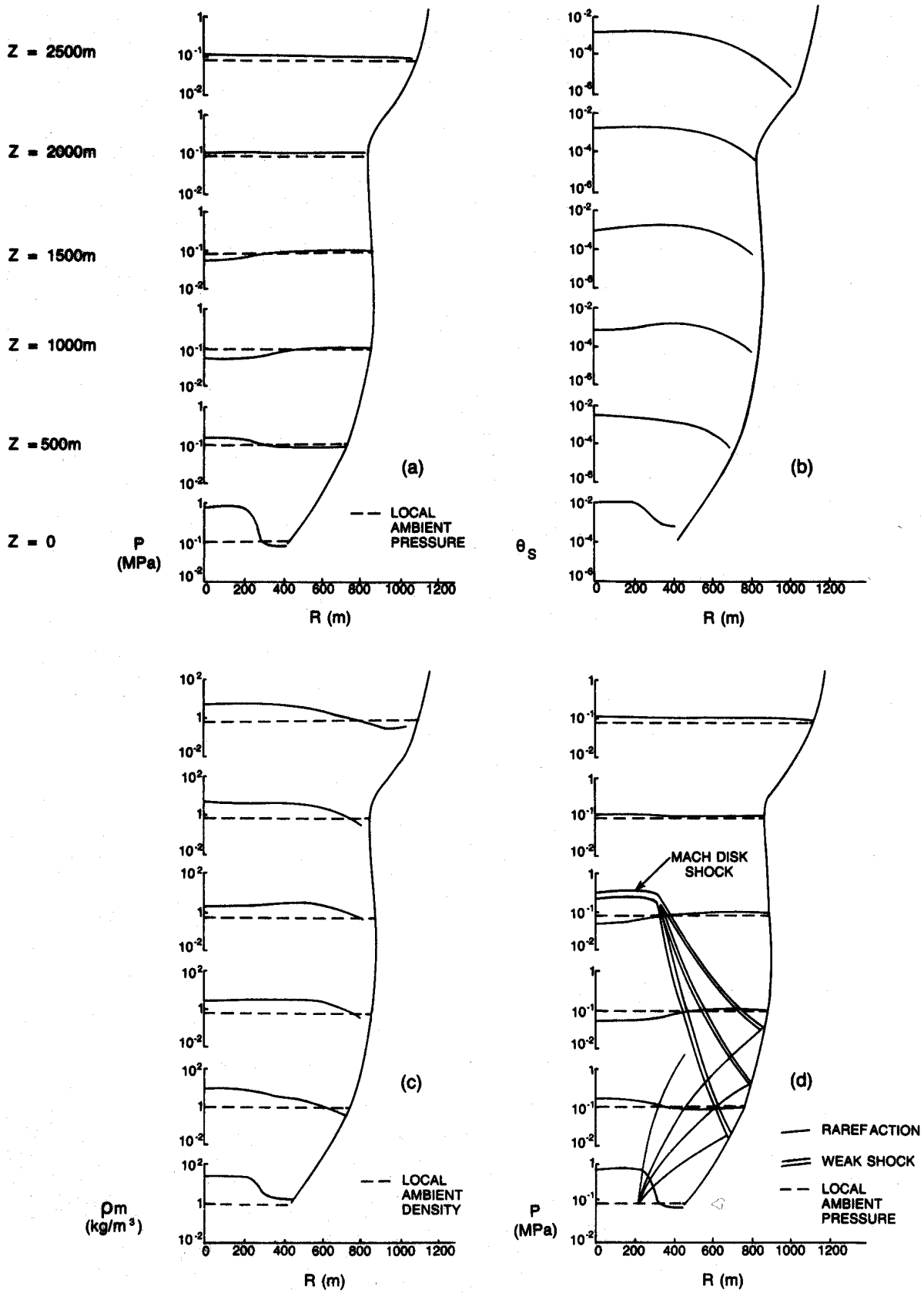

Fig. 6. Detail of the basal 2.5 km of the overpressured eruption shown in Figure 3. Radial variations of (*a*) p, (*b*) θ_s, and (*c*) mixture density ρ_m are plotted at 500-m intervals above the exit plane. (*d*) How oblique rarefactions and shocks interact with the flow to produce the observed dynamics. See text for detailed discussion.

from experiments with overpressured jets [*Chemical Propulsion Information Agency*, 1975; *Kieffer*, 1984; *Kieffer and Sturtevant*, 1984] and detailed numerical modeling of jets [*Norman et al.*, 1982]. This previous experimental and numerical work has shown that overpressured, supersonic jets flare rapidly upon exiting their nozzles (vents) and expand by the Prandtl-Meyer process. Oblique rarefactions reflect off the edges of the jets to form weak converging shocks. The shocks

meet at some distance downflow of the nozzle exit and form a strong shock that is parallel to the exit plane (Mach disk shock). Approximate locations of rarefactions and shocks in the model run discussed above are shown in Figure 6*d*; these are based upon analogous laboratory experimental data and are not directly derived from the numerical model. Rarefaction zones are well represented in the numerical model because in reality they are zones of smooth pressure gradients. Shocks, on the other hand, are nearly discontinuities in real gas flows. However, in the numerical results they are smeared out over larger distances than would be expected in nature due to numerical diffusion [*Hirt*, 1968]. In addition, the presence of particles in a gas flow produces an effective thickening of shocks because, although the properties of the gas itself undergo a sharp discontinuity, the imperfect coupling of particles and gas requires a finite distance for the particles to regain equilibrium with the gas [*Carrier*, 1958; *Rudinger*, 1960; *Marble*, 1970]. Thus there are no sharply defined shocks produced by the numerical model, which instead shows regions of rapid compression, illustrated as shocks drawn in Figure 6*d*.

Collapsing column (fountain). Figure 4 shows the evolution of an example collapsing eruption column and resulting pyroclastic flow (run 8; see Table 2). This eruption plots below the critical surface of Figure 5 and is in pressure equilibrium with the atmosphere at the exit plane.

At $t = 10$ s the working surface is between 2 and 3.5 km elevation (Figure 4) with velocity vectors showing development of a rolling vortex in this region (not visible in the small reproduction shown in Figure 4). The velocity vectors also show a rapid deceleration toward the top of the column along the r axis. This deceleration produces high-pressure regions in the flow as kinetic energy is converted to internal energy (manifested as pressure). The atmospheric pressure signal is about 5 km from the vent at 10 s and out of the computational domain a few seconds later.

At $t = 80$ s the column has spread laterally at an elevation of about 3.5 km, and that part of the flow is beginning to collapse toward the ground. At the elevation of collapse, vertical velocity along the axis of symmetry has decreased to zero, resulting in a high-pressure (and high gas density) cell. Also noteworthy is the difference between the shapes of the bases of the eruption columns shown in Figures 3 and 4. The model in Figure 4 exits at atmospheric pressure and does not display the flaring property of the run in Figure 3. Note the well-developed vortex above the front of the collapsing flow (here referred to as the "stem"). Also note that significant quantities of ash continue to rise above the forming fountain. This observation is consistent with observations from modern eruptions and serves to point out a difficulty in using cloud shape to determine whether or not a column is collapsing. If a column is undergoing asymmetrical collapse, an observer on one side may witness collapse and resulting pyroclastic flows, while an observer on the other side will only see a steadily rising plume of ash. Thus two radically different interpretations of eruption dynamics could result from real-time observations of the same eruption, and it is expected that pyroclastic flow deposits and fallout deposits may form contemporaneously (this possibility is suggested from field observations of deposits from the 1912 eruptions of Novarupta [*Hildreth*, 1987]).

By $t = 140$ s, pyroclastic flows are moving laterally across the ground. A high-pressure cell is present where the collapsing stem impinges on the substrate, reflecting rapid deceleration and conversion of kinetic energy into internal energy. The gas density plot shows that the collapsing flow results in injection of less dense, hot gas beneath a relatively cooler and denser atmosphere. There are two components of pyroclastic ground flow: one component moves outward, while the second component of pyroclastic flow moves inward toward the vent. At 140 s the inward moving component is just beginning to meet the main column, where later it is reincorporated into the column. This phenomenon may produce considerable recyclng of material during the course of an eruption, a possible consequence being the mixing of earlier erupted ash with later products. This process has not been documented in the field, but it may be responsible for obscuring temporal magma compositional changes that otherwise might be preserved by vertical zonation of the pyroclastic deposit. For example, a sharp compositional interface in the magma chamber might be smeared out stratigraphically in corresponding ignimbrite, so that it may be incorrectly interpreted as having been a smooth compositional gradient. Whether this remixing process occurs during an eruption depends, for example, on the slope away from the vent. Where a collapsing stem impinges on an outward dipping slope, the inward flowing part may produce a pyroclastic flow with insufficient momentum to flow up the slope toward the vent. Also, as will be discussed in a later section, clast sizes control the distances from the vent at which collapsing stems hit the ground. Coarse material collapsing very close to the vent can effectively damp out the backflow.

IMPLICATIONS FOR PYROCLASTIC FLOW TRANSPORT AND IGNIMBRITE FACIES

Results of the numerical experiments are not appropriate for application to outcrop features smaller than the 100-m computational grid. Most features observed on the outcrop scale are strongly influenced by the detailed rheology of pyroclastic flows [*Sparks*, 1976; *Wilson*, 1980; *Wilson and Head*, 1981; *Freundt and Schmincke*, 1986; *Valentine and Fisher*, 1986; *Beget and Limke*, 1988]. In our multiphase treatment, bulk fluid properties are essentially Newtonian, and a detailed treatment of pyroclastic flow mechanics could incorporate granular flow dynamics [*Savage*, 1984]. The strength of our model is that it sheds light on the large-scale features of an eruption, and the interpretations presented below pertain only to broad facies relationships commonly observed in pyroclastic flow deposits (see reviews by *Fisher and Schmincke* [1984, pp. 203–206] and *Cas and Wright* [1987, pp. 244–250]).

Pyroclastic Flows

The structures of model pyroclastic flows reflect important physical processes that control runout of pyroclastic flows and ignimbrite facies. In addition to the results of run 8, shown in Figure 4, three other examples of fountains (runs 19, 59, and 61) are shown in Figures 7–9, where θ_s and velocity vectors are plotted at three times. Conditions for these runs are given in Table 2, and the main variations relative to the run in Figure 4 are a short eruption discharge duration (50 s) for run 19, large particle Rouse number (particles are equivalent to 10-cm-radius lithic fragments) for run 59, and low Tg_m and Ri_m in run 61.

Pyroclastic flows produced by brief discharge. Figure 7 (run 19) shows the development of a pyroclastic flow and its evolution after discharge has ended. This has relevance for pyroclastic flows produced by relatively brief periods of column collapse either from eruptions consisting of discrete explosions

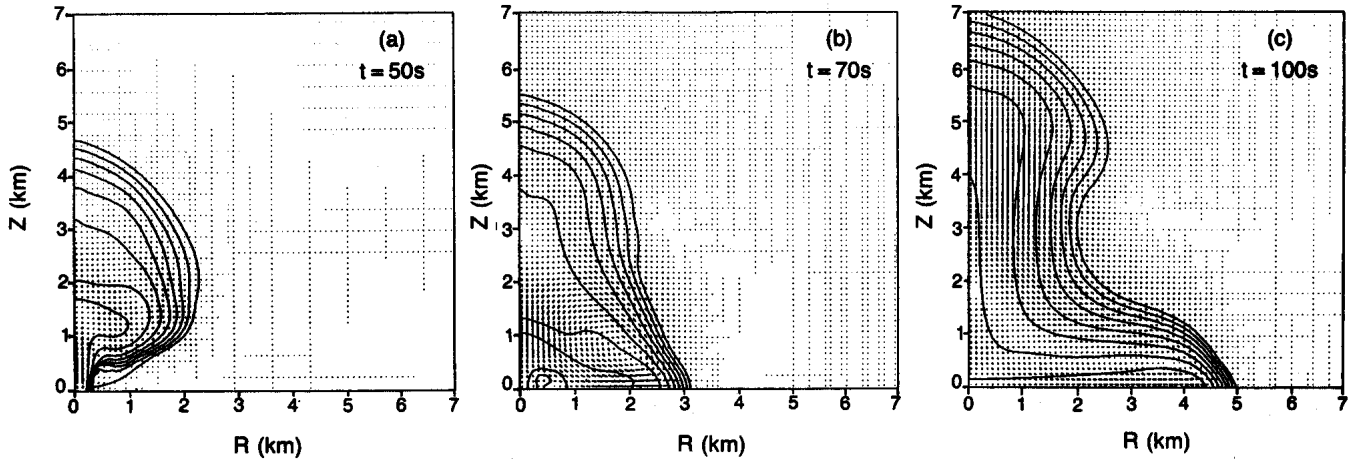

Fig. 7. The log θ_s-$\mathbf{u}_s$ plots of the flow field produced by a brief discharge duration (run 19). At $t = 50$ s, discharge is "turned off," and the flow is producing a collapsing fountain. Although the bulk of material in the eruption cloud produces laterally moving pyroclastic flow, a buoyant cloud of ash continues to rise above the vent, attaining upward speeds in excess of 50 m/s. Note the well-developed vortex above the head of the pyroclastic flow, especially evident at $t = 70$ s, and that maximum velocities in the ash plume occur away from the symmetry axis.

or from sustained Plinian eruption columns with brief periods of instability (producing intra-Plinian pyroclastic flows [*Wright*, 1981; *Wilson and Walker*, 1985; *Walker*, 1985]). At $t = 50$ s the column begins to collapse at an elevation of about 2 km, and the eruption discharge is "turned off"; 20 s later, at $t = 70$ s, most of the erupted material (contained within the innermost θ_s contour) is falling back to the ground and moving outward as the beginning stages of pyroclastic flow. Note the strong vortex development on top of the pyroclastic flow and that ash continues to rise immediately above the vent. The final snapshot in Figure 7 ($t = 100$ s) shows the development of a pyroclastic flow with a relatively thick head that tapers gradually ventward to a lower-concentration tail. The head of the pyroclastic flow consists of a relatively low-concentration front and a well-developed vortex along its top. One might expect the deposits of such an eruption to reflect an initial low concentration phase, followed by a higher-concentration phase, and ending with another low-concentation phase. Note the cloud of buoyant ash rising above the vent with relatively high velocities between about 3 and 6 km elevation. This phenomena suggests that it would be difficult to determine exactly when discharge ends based on field observations of eruption column dynamics.

Pyroclastic flows produced by coarse-grained eruption. Figure 8 shows run 59 at $t = 90$, 115, and 135 s. This model eruption consists of clasts of large Rouse number (10-cm radius, density of 2400 kg/m^3), so that interphase coupling is extremely poor. Note that this eruption has the same mixture parameters at the vent as run 49. Run 49 (Figure 3) produced a Plinian column, and run 59 produced a fountain, which demonstrates the effect of *Pn* on eruption dynamics.

Because of the poor coupling between the solid and gas phase caused by large Rouse number, run 59 permits observation of the development of density-current structure. At 90 s the collapsing stem of the column has a well-developed head, caused by resistance of the atmosphere into which it is flowing and by drag associated with vortex flow. When $t = 115$ s, the stem has just impinged on the ground, and by $t = 135$ s, pyroclastic flows are moving rapidly outward and inward. Note that the inner contour of the pyroclastic flow, where the densest part of the flow exists, displays a thickened head with a slight overhang at its front. This is a common feature of den-

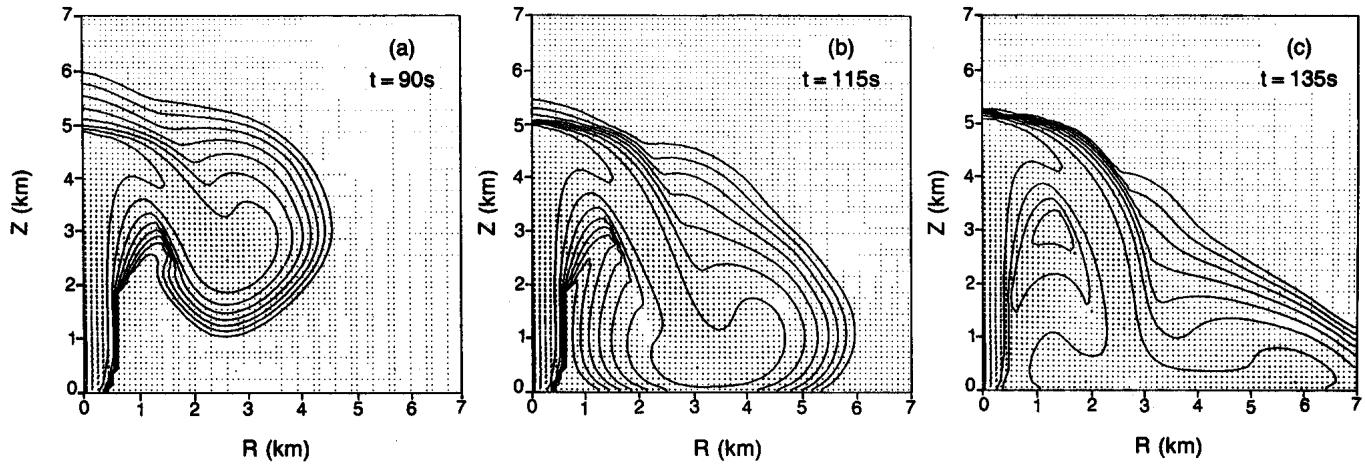

Fig. 8. The log θ_s-$\mathbf{u}_s$ plots of coarse-grained eruption (run 59). Because of poor coupling between the gas and solid phases, structure of the pyroclastic flow is well illustrated by the innermost contour of the lateral flow. A relatively thick head with a slight overhang is shown, followed by a relatively thinner body of the flow.

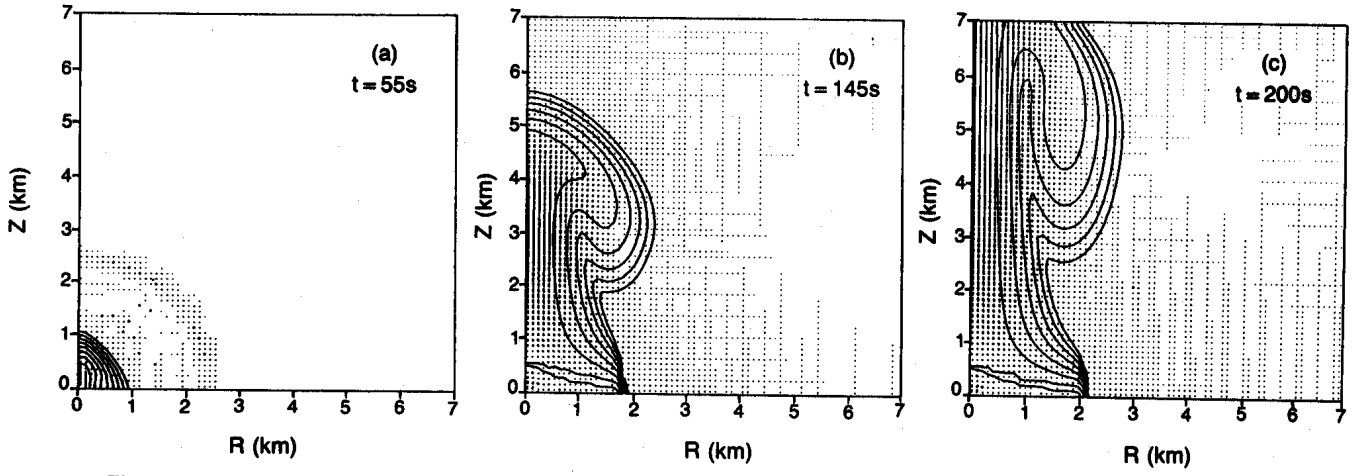

Fig. 9. The log θ_s-$\mathbf{u}_s$ plots of a relatively weak eruption (run 61). Most of the pyroclastic material rises only 300 m above the vent, then moves laterally as a slow pyroclastic flow. However, a buoyant plume of ash continues to rise above the vent at relatively high speeds approaching 120 m/s (note the exit velocity is only 73 m/s). This rising ash cloud produces a strong radially inward flow in the atmosphere, which exerts sufficient drag on the pyroclastic flow to effectively stop its progress.

sity currents produced by laboratory experiments [*Hampton*, 1972; *Allen*, 1970, pp. 189–192], lending credence to the numerical model presented here. This structure also supports ideas put forth by *Wilson* [1980, 1985], and *Wilson and Walker* [1982] on the geometry of pyroclastic flows.

At later times in the run of Figure 8, the dilute cloud that occurs above the pyroclastic flow gradually collapses toward the ground until it is less than 2 km thick. Compare this to runs with lower-*Pn* particles, which produce buoyant, continuously rising ash clouds (discussed in detail below). This difference again is a reflection of the coupling between particles and gas.

Pyroclastic flows produced by low Tg_m-Ri_m-K_p eruption. Figure 9 shows run 61 at three times. As can be seen in Table 2, this run has relatively low values of Tg_m and Ri_m and is pressure-balanced at the exit plane. In addition, the Rouse number of the particle phase is low. These conditions correspond to natural conditions of low energy eruption in which eruptive products appear to "boil" over the vent rim (e.g., the eruption of Mount Lamington described by *Taylor* [1958]).

Most of the material erupted during run 61 rises only to 200–300 m above the vent, then collapses to form a slow moving pyroclastic flow. A low-concentration cloud of ash continues to rise above this level; the beginning stages of this cloud are seen in the plot for $t = 55$ s. After 145 s of discharge the pyroclastic flow has only moved a total of about 2 km away from the vent. The buoyant ash cloud, however, is rising very rapidly, resulting in a strongly radially inward wind as the atmosphere is dragged up with the cloud. By $t = 200$ s the inward wind produced by ash cloud rise is exerting enough drag on the low-energy pyroclastic flow to effectively halt its progress. Material initially flowing outward in the pyroclastic flow is gradually fed into the head of the flow and then sucked up into the buoyant ash cloud. Thus we see that for a pyroclastic flow to make any appreciable lateral progress, it must have enough inertia to counteract the inward wind produced by the convective rise of the ash cloud above the vent.

The results of run 61 point to yet another problem with field observation of eruptions. An eruption that produces a very low energy pyroclastic flow that is prematurely halted by wind drag may appear to be entirely Plinian, especially if near-vent topography or suspended ash hides the flow. Obviously, this would result in a gross misinterpretation of the energetics of that eruption.

Ground Surge

Basal deposits of ignimbrites commonly display features of pyroclastic surge deposits, such as improved sorting relative to pyroclastic flow deposits and cross stratification. These basal deposits were termed "ground surge" by *Sparks and Walker* [1973], and were placed in the layer 1 position of the "standard" ignimbrite sequence of *Sparks et al.* [1973] and *Sparks* [1976]. Subsequent variants of layer 1 deposits include ground layers and fines-depleted ignimbrite [*Walker et al.*, 1981; *Wilson and Walker*, 1982]. In addition, deposits that record turbulent boundary layer processes in pyroclastic flows have been predicted by *Valentine and Fisher* [1986].

Layer 1 deposits that fall into the category of ground surge have been interpreted in terms of three models. First, *Wilson and Walker* [1982] suggest that ground surge deposits are associated with unsteady processes at the fronts of pyroclastic flows. Second, *Wohletz et al.* [1984] present numerical modeling that suggests ground surges may be related to initial unsteady flow and blasting phenomena at the beginning of an eruption. The third model [*Fisher*, 1979] suggests that these deposits record the initial stages of eruption column collapse. In Fisher's scenario, the outer sheath of the eruption column has a lower particle concentration and is finer-grained than its core. The lower concentration is postulated to be due to mixing with ambient air, and the fine-grained property is due to size grading inherited from the conduit flow. The model assumes that when column collapse begins the outer sheath of the column collapses first, producing fine-grained, low-concentration pyroclastic surges that are subsequently followed by denser, coarser-grained pyroclastic flows.

Numerical modeling by *Ishii et al.* [1987] of gas-particle flows moving through diverging nozzles shows that the outer parts of the flows have lower particle concentrations because of the relatively slow response of the particles to the nozzle shape, compared to the nearly instantaneous response of the gas. Thus if a volcanic eruption occurs through a flaring vent one might expect higher particle concentrations and coarser

sizes in the core of the eruption column flow than at its edges, supporting ideas put forth by *Fisher* [1979]. The DASH models also indicate this concentration gradient, but they do not directly support the idea that the outer sheath of the column will collapse before the core. Instead, at the elevation of collapse, the entire cross section of the column "flops" downward at the same time. Still, as illustrated in Figure 4, the lower-concentration outer part of the column is pushed in front of the higher-concentration core material during initial collapse. The result is that lower concentration parts of the flow hit the ground first and then continue to move laterally in front of higher-concentration parts (note that this effect is exaggerated somewhat in the numerical experiments due to numerical diffusion [*Hirt*, 1968]). It is possible that this leading part of the flow may have characteristics of pyroclastic surges, and thus lay down bedded and cross-bedded deposits just prior to the main pyroclastic flow. This is more likely to be an active process near the vent, because with increasing runout distance the low-concentration front may be stripped off by aerodynamic drag on the pyroclastic flow and may possibly be overtaken by the dense pyroclastic flow.

Ash Cloud

The presence of a dilute ash cloud above model pyroclastic fountains and related pyroclastic flows, mentioned several times in the preceding discussion, has several important implications. In Figure 4 at $t = 140$ s, notice the cloud of ash rising above the fountain and pyroclastic flow. This dilute ash cloud flows back toward the axis of symmetry by convective inflow of the atmosphere, and then rises to form a buoyant plume analogous to the ash cloud discussed by *Fisher* [1979] (see also documented ash clouds from the May 18, 1980, eruption of Mount St. Helens by *Criswell* [1987]). The ash cloud is thought to deposit a "coignimbrite ash," layer 3 of the standard ignimbrite sequence of *Sparks et al.* [1973]. Fine ash layers at the tops of pyroclastic flow units have been described at numerous locations [*Wilson and Walker*, 1985; *Wilson*, 1985; *Bacon*, 1983; *Sparks*, 1976; *Fisher*, 1979]. Recently, *Rose and Chesner* [1987] suggested that the voluminous 75 ka Toba eruption generated several hundred cubic kilometers of this coignimbrite ash. Layer 3 has been attributed to sorting of fine ash in collapsing eruption columns and elutriation of fine ash from the dense pyroclastic flow [*Sparks and Walker*, 1977; *Wilson*, 1980]. *Denlinger* [1987] finds that turbulent boundary layer and granular flow processes act together to produce ash clouds. Layer 3 seems to have been deposited by fallout in some cases and by lateral transport in others (i.e., ash cloud surge of *Fisher* [1979]).

DASH results indicate the following interpretation. Ash may rise buoyantly above the main pyroclastic flow, carried by rising hot gas (fluidization [*Wilson*, 1980, 1984]) and by diffusive processes such as turbulence [*Denlinger*, 1987]. The rising ash forms a relatively low-concentration cloud that flows inward, relative to the main pyroclastic flow, toward the main axis of the eruption column. As mentioned above, this is largely due to drag from atmospheric wind that is pulled inward and upward with the eruption column. The majority of ash cloud material rises buoyantly and is later deposited by fallout. Coarser tephra may be deposited during the backflow of the ash cloud, resulting in dunes and other features typical of pyroclastic surge deposits on top of pyroclastic flow units. In this fashion, dunes recording crest migration toward the vent are not necessarily antidunes, because their parent flow (the ash cloud) may itself have been flowing toward the vent relative to the underlying pyroclastic flow.

This backflow phenomenon is predicted by DASH for only near-vent locations. As radial distance increases, ash clouds may become detached from the parent pyroclastic flow and move unaffected by backflow and also can continue flowing after the pyroclastic flow itself has come to a stop (see discussion by *Denlinger* [1987]). Farther away from the vent, and for small eruptions, the inward flowing wind decreases so that the ash cloud would be able either to rise vertically, move entirely according to its own momentum, or be blown by the nonvolcanic wind in any direction.

Proximal Coignimbrite Breccias and the Deflation Zone

Previous work. The numerical modeling presented here has an important bearing on near-vent processes that produce proximal breccias often observed to be related to ignimbrites. Detailed descriptions of proximal breccias have been given by *Wright and Walker* [1977, 1981], *Wright* [1981], *Druitt* [1985], *Druitt and Sparks* [1982], *Druitt and Bacon* [1986], *Bacon* [1983], *Caress* [1985], *Kite* [1985], and *Freundt and Schmincke* [1985]. Various terms have been used for these deposits and each term corresponds to a specific flow/emplacement mechanism (see below). We use the term "proximal coignimbrite breccia' as a nongenetic name for lithic-rich breccias that are found in proximal areas around ignimbrite vents and are laterally equivalent to or associated with ignimbrites. Proximal coignimbrite breccias originate by the same eruptive event as their laterally equivalent ignimbrites. This discussion pertains to outflow ignimbrite only, and does not consider intracaldera breccia formation [*Lipman*, 1976].

Proximal coignimbrite breccias were first discussed by *Wright and Walker* [1977] and were termed by them "coignimbrite lag fall" deposits. They were interpreted by *Wright and Walker* [1977, 1981] to represent deposition of heavy clasts at the site of column collapse. The term "lag fall" reflects the idea that the breccia material falls from the eruption column and lags behind the remainder of the material that coalesces to form pyroclastic flows. *Walker* [1985] simplified the term used for these deposits to "lag breccia" and proposed a model whereby the breccias are deposited from a highly expanded, turbulent zone around a collapsing eruption column. This zone, called the "deflation zone," was postulated by *Sparks et al.* [1978] and *Sparks and Walker* [1977] to be the site where dense pyroclastic flows are actively segregating from a low-concentration flow. *Druitt and Sparks* [1982] observe that coarse, poorly sorted, clast-supported breccias vertically and laterally grade into ignimbrite and that the breccias are laterally equivalent to layer 2bL, the lithic concentration zone commonly found near the base of ignimbrite flow units [*Sparks et al.*, 1973]. In the above models, sorting of proximal breccias is attributed to gas streaming, analogous to fluidization, during lateral flowage of the material.

The significance of proximal breccias in terms of eruption dynamics has been discussed by *Druitt and Sparks* [1984], *Druitt* [1985], and *Walker* [1985]. These workers suggest that the occurrence of proximal breccias within a caldera-forming eruption sequence marks the onset of caldera collapse. In addition, *Walker* [1985] proposes that variations in the extent of proximal breccias in a given eruption sequence are related to variations in the extent of the deflation zone due to discharge

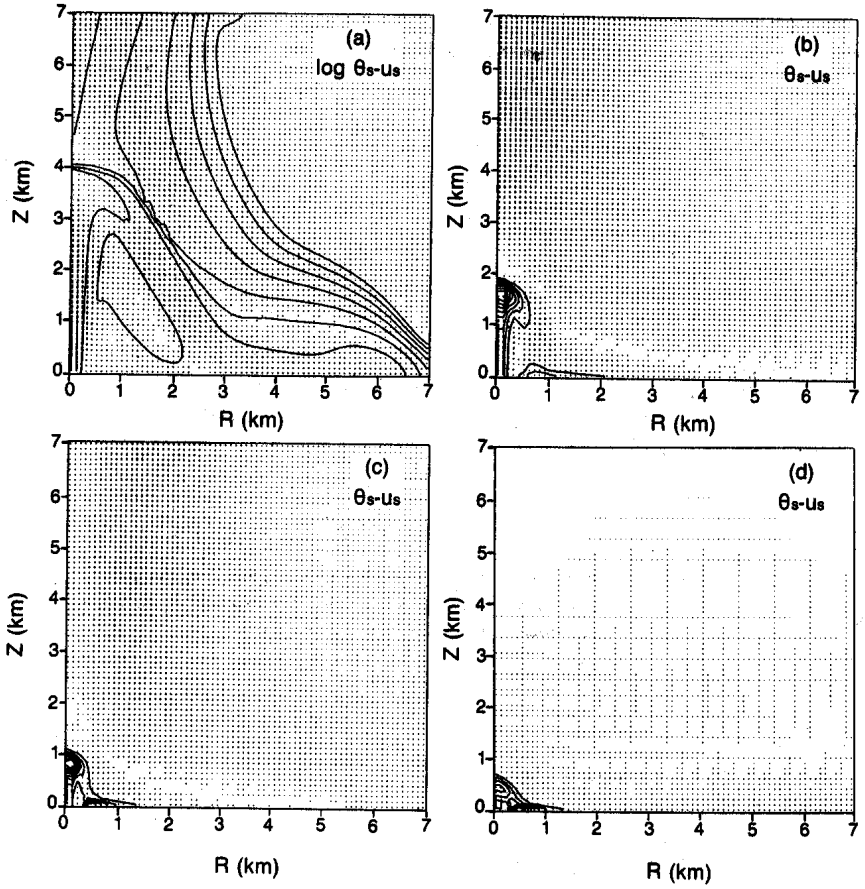

Fig. 10. Ash volume fraction and velocity plots for eruptions at late time (t = 185 s), demonstrating how pyroclastic flow dispersal depends upon Rouse number (Pn). The only parameter that varies between these eruptions is the particle size. (*a*) The log θ_s-$\mathbf{u}_s$ plot of run 8 (same as Figure 4), with $Pn = 0.028$. Pyroclasts rise to about 3.5 km elevation and impinge upon the substrate at a distance of about 2.5 km from vent. (*b*) The θ_s-$\mathbf{u}_s$ plot of run 46, $Pn = 0.088$, shows pyroclasts rising only to 1.1 km and impinging upon the ground at 0.6 km from vent center. (*c*) The θ_s-$\mathbf{u}_s$ plot of run 40, $Pn = 0.28$, where material rises to 0.7 km elevation and hits the ground at 0.5 km from vent center. (*d*) The θ_s-$\mathbf{u}_s$ plot of run 43, $Pn = 0.88$, with pyroclasts rising to 0.4 km elevation and hitting the ground at 0.3 km from vent center. Note that only Figure 10*a* plots contours of log θ_s: Figures 10*b*–10*d* plot θ_s, since the poor coupling between the gas and solid phases in these runs limits pyroclast dispersal. The log θ_s plots of Figures 10*b*–10*d* would only show one contour.

fluctuations. *Druitt* [1985] suggested that the formation of proximal breccias is at least partly due to overpressured conditions at the vent which enhance vent erosion. He suggests that this condition will be met during periods of rapidly increasing discharge, such as the onset of caldera collapse.

Modeling approach and results. In order to examine the behavior of various clast Rouse numbers we have run the DASH code with clast radii ranging from 10^{-4} to 10^{-1} m. To isolate the effects of particle characteristics alone, experiments were designed to compare eruptions with different particle radii but with identical mixture parameters, so that Pn was varied while Tg_m, Ri_m, K_p, and Ds were held constant. Referring to Table 2, the runs discussed here are 8, 40, 43, and 46.

Figure 10 shows the θ_s-velocity plots for four experiments at late stages of column collapse (t = 185 s). Two general results are illustrated: (1) collapse height varies inversely with Pn, and (2) higher-Pn clasts hit the ground much closer to the vent than their finer counterparts. For example, fine ash is transported to about 3.5 km above the vent and falls to the ground at a radial distance of about 2.5 km, while 1-cm-radius lapilli move only to 0.7 km and fall to the ground at about 0.5 km from the vent center. 10-cm lithic fragments return to the ground at only 300 m from the center of the vent. Not surprising from a physical standpoint, these results simply reflect the degree to which particles are coupled with the gas phase in an eruption (see also discussion by *Wilson et al.* [1987]). Very fine particles are nearly perfectly coupled with the gas. They are dragged up much higher before the mixture density causes instability and collapse. Large particles, on the other hand, are barely affected by gas drag and follow paths that are more nearly ballistic. In reality, large clasts will experience an increased drag force caused by the presence of fine particles suspended in the gas. Thus the results of the present numerical modeling can not be exactly applied to natural eruptions. Nonetheless, these experiments show the relative effects of varying Pn, and we feel that the results apply qualitatively to real eruptions. Furthermore, the above results indicate that the sorting observed in proximal breccias is primarily inherited from the eruption column itself and that gas sorting during lateral flowage is a second-order process.

Numerical experiments for all Pn show the formation of pyroclastic flows that consist of inwardly and outwardly moving parts, as was discussed in an earlier section. The finest material involved in collapse will fall to the ground at the largest distance from vent, and all pyroclastic flows outside of this distance will move away from the vent. What happens inside this envelope in a real eruption, however, is not clear. Some backflow of finer material into areas where coarser ma-

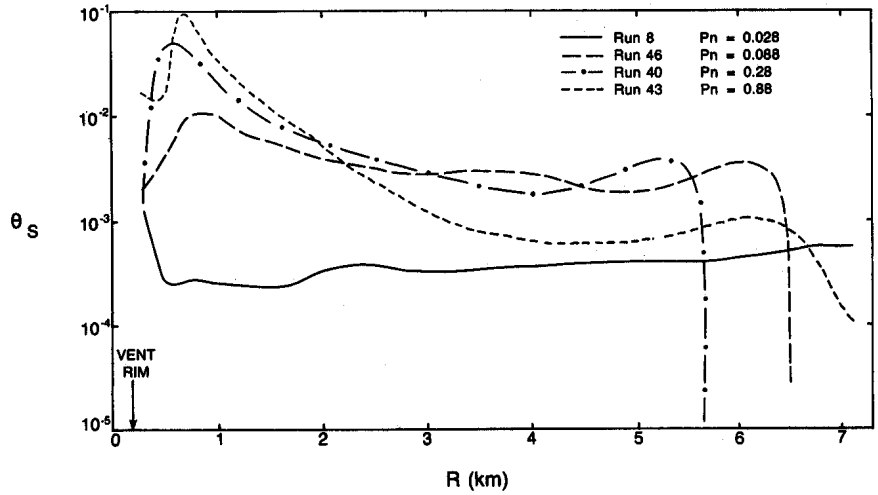

Fig. 11. Solid volume fraction (θ_s) plotted against radial distance from vent center for the model eruptions shown in Figure 10 ($t = 185$ s). Peaks in θ_s between 0 and 3 km from vent center correspond to sites where collapsing flow is impinging upon the ground, so that the proximal area is the area of highest pyroclast concentration. This runs contrary to the deflation zone concept. Note that runs 46, 40, and 43 each have second maximum in θ_s between 5 and 7 km from the vent. These features are associated with the heads of the individual pyroclastic flows.

terial is falling will lead to some mixing of the two. On the other hand, very close to the vent, the coarsest material having followed nearly ballistic paths may flow radially outward where it may mix with progressively finer material. During flow away from the vent, coarse clasts become progressively diluted because of two processes: (1) sedimentation out of flow, and (2) mixing with increasing quantities of finer clasts.

This simple analysis of model results can explain most features of proximal coignimbrite breccias described by previous authors. Some deposits, especially those extremely close to vent, may be expected to have characteristics of fallout deposits, such as continuous bedding and good sorting [*Wright and Walker*, 1977, 1981]. These deposits would indeed be true fallout because they simply "piled up" where the material hit the ground. However, our models show that much of the material can continue to flow after falling to the ground, producing discontinuous stratification and mixing with finer and less dense material. In places, coarse-grained flows originating from the vent may move over newly deposited, finer, pumiceous ash. If the coarse-grained flows are lithic rich, they will be much denser than the underlying ash deposit, and pods and rafts of lithic breccia may sink down into the underlying material [*Druitt and Sparks*, 1982]. This situation is expected to enhance degassing of the underlying ash resulting in increased formation of degassing pipes.

Plots of maximum lithic size versus distance from vent commonly show inflection points [*Wright and Walker*, 1977; *Wright*, 1981; *Wilson*, 1985; *Druitt and Bacon*, 1986; *Caress*, 1985]. These inflections are suggested by the above authors to mark the outer edge of the postulated deflation zone. In contrast, the DASH models suggest that the inflection simply represents the runout distance of coarse breccia material as defined by its potential energy line [*Sheridan*, 1979]. Beyond that point, transport is determined by the pumice flow, which may carry lithics and undergo grading processes as discussed by *Sparks* [1976] and many other authors.

In summary, the main result of our numerical models regarding proximal coignimbrite breccias is that the concept of the deflation zone is not supported. In fact, the modeling indicates that the near-vent region will have the highest particle concentration ground flow, as opposed to being very low concentration as postulated for the deflation zone concept (Figure 11).

CONCLUSIONS

Numerical models of Plinian eruptions have been made in which the full set of Navier-Stokes equations are separately solved for solid-particle and gas phases in two dimensions. These models provide direct analysis of some basic nonlinear processes active in eruption columns. The main results of the analysis of 51 numerical experiments are as follows:

1. The most fundamental types of eruption column behavior, high-standing Plinian and collapsing fountain, are determined by the density and velocity of the erupting mixture, the exit pressure, and the vent radius. The critical conditions for eruption column collapse form a surface in Tg_m-Ri_m-K_p space for eruptions with similar grain size characteristics. Column behavior is more strongly influenced by the ratio of exit pressure to ambient pressure than by the ratio of column density to ambient density within the framework of this numerical model.

2. Overpressured eruptions display features that are observed in laboratory experiments of overpressured jets. The erupting mixture initially expands and accelerates above the vent, then compresses and decelerates through a Mach disk shock. This process produces a characteristic diamond-shaped cross section at the base of eruption columns.

3. Pyroclastic flows can consist of two parts. One part flows outward from the vent to form outflow facies tuff; the other part may flow toward the vent and thus result in recycling of erupted material back into the column. Pyroclastic flows produced by the numerical model display a relatively thick head, a thinner body, and a lower-concentration tail. This structure corresponds well with laboratory density currents. In order to flow away from the vent, a pyroclastic flow must have enough momentum to overcome the drag of convectively inflowing atmosphere. Insufficient momentum may result in a weak pyroclastic flow eruption with only a towering ash cloud visible to the observer.

4. The numerical experiments suggest that during the beginning stages of eruption column collapse, lower-concentration outer parts of the column may be pushed ahead

of higher-concentration parts. When the material impinges on the ground, the result is a pyroclastic flow with a low-concentration front. This may lead to deposition of the ground surge deposit commonly observed beneath pyroclastic flow deposits.

5. Buoyant, low-concentration clouds of ash that rise above fountains and related pyroclastic flows are observed in all eruptions (excepting those in which the particles are very coarse). In proximal areas (within 7 km from vent) the ash clouds typically flow toward the vent relative to the main pyroclastic flow. Deposits from the inflowing ash cloud may show ventward migrating dunes. In natural eruptions it is likely that the ash cloud may obscure pyroclastic flow processes and lead to misinterpretation of eruption dynamics. It is also expected that fallout deposits may form concurrently with pyroclastic flows, so that caution must be used in interpreting deposits in terms of eruption processes.

6. The model supports an origin of proximal coignimbrite breccias by sorting within the eruption column. In this case, coarser clasts collapse from the column at lower elevations and hit the ground closer to the vent than finer clasts. The breccias become finer-grained with distance mainly due to sorting that occurs before hitting the ground instead of during lateral flowage. Lateral flow of all the material spreads the clast size distribution laterally over greater distances than the vertical distribution in the eruption column. It is suggested that the inflection point commonly observed in maximum-lithic-size versus distance-from-vent plots is related to the potential energy line of the breccia material.

7. The numerical model does not support the existence of a "deflation zone" in proximal areas around a fountain, as has been suggested by previous authors. Instead, pyroclastic flows in this area appear to have a higher concentration than any other location in the computational domain.

APPENDIX: SCALING OF VISCOUS FORCES AND HEAT CONDUCTION

Scaling of Viscous Effects

Viscous effects have been omitted from the discussion of dimensionless parameters and the significance of those parameters with respect to eruption dynamics. As shown here, viscous forces are negligible compared to the other forces represented in equations (16)–(18).

We apply the pseudogas (or dusty gas) approximation to the flows in order to calculate an effective kinematic viscosity [*Marble*, 1970]:

$$v_{dg} = \frac{v_g}{1 + m} \tag{A1}$$

where v_g is given in Table 1 and m is the mass ratio of solids to gas. In the numerical experiments, θ_s ranges from 10^{-1} to 10^{-3} at the exit plane, corresponding to m between 1500 and 10. Values of v_{dg} vary accordingly from about 7×10^{-8} to 7×10^{-6} m^2/s. To determine the relative importance of viscosity, we form ratios with inertial, buoyancy, and thermodynamic forces.

The ratio of inertial forces to viscous forces is given by the Reynolds number (Ry) in the following form:

$$Ry = uL/v_{dg} \tag{A2}$$

where u and L are the characteristic velocity and length, respectively. We take $u \sim 100$ m/s and $L \sim 100$ m. Thus for the range of θ_s in this work, we have $Re \sim 10^{12}$ to 10^{10}, which demonstrates that viscous forces are negligible compared to inertial forces.

The ratio of buoyancy forces to viscous forces forms the Archimedes number (Ar), given by

$$Ar = \frac{(Ds - 1)gL^3}{Ds^2 v_{dg}^2} \tag{A3}$$

For the range of conditions considered in this work, we find that the smallest value of the Archimedes number is $Ar \sim 10^{16}$, showing that viscous forces are also negligible compared to buoyancy forces.

A ratio of thermodynamic (pressure) forces to viscous forces is given by

$$\frac{L^2(\Delta p)}{\rho_m v_{dg}^2} \sim 10^{15} \tag{A4}$$

where Δp is a characteristic pressure change, taken as $\Delta p \sim 0.1$ MPa. Thus it is clear that the true viscosity of the flows plays a negligible role in the dynamics relative to other types of forces. This justifies our neglect of viscous forces throughout the paper.

Scaling of Intraphase Heat Conduction

Intraphase heat conduction (heat conduction within individual phases) is not computed in the numerical model used for this work. To justify this, we examine the magnitude of conductive heat transport relative to other forms of heat transport in equation (3). Since the solid phase is treated as dispersed particles, intraphase heat conduction is irrelevant. The gas phase, however, is continuous and requires an order of magnitude estimate of heat conduction. For this purpose we have

$$q = k_g \frac{dT}{dz} \tag{A5}$$

where the direction of heat transport is irrelevant. For a typical temperature gradient of 1 K/m (or 100 K per computational cell) and k_g from Table 1, we get $q \sim 0.5$ W/m^2. The ratio of advective heat transport to conduction is

$$\frac{u(\rho_g c_{vg} T_g)}{q} \sim 10^7 \tag{A6}$$

where $u \sim 100$ m/s, $\rho_g \sim 0.1$ kg/m^3, and $T_g \sim 100$ K. The ratio of energy transport due to pressure changes (work) to conduction is

$$\frac{pu/L}{q} \sim 10^6 \tag{A7}$$

for $p \sim 0.1$ MPa. The ratio of interphase heat transfer to intraphase conduction is

$$\frac{R_s L}{q} \sim 10^{10} \tag{A8}$$

for velocity and temperature differences (Δu and ΔT) between particles and gas of 10 m/s and 10 K, respectively, $\theta_s = 10^{-2}$, and $r = 10^{-4}$ m. Finally, the transfer of energy from interphase drag is proportioned to conductive transfer as

$$\frac{K_s(\Delta u)^2 L}{q} \sim 10^8 \tag{A9}$$

Thus we see that intraphase heat conduction in the gas is negligible compared to the other energy transport mechanisms.

NOTATION

a radiation absorptivity.
Ar Archimedes number, ratio of buoyancy forces to viscous forces.
c_m sound speed, LT^{-1}.
c_d drag coefficient.
c_p heat capacity at constant pressure, $L^2T^{-2}K^{-1}$.
c_v heat capacity at constant volume.
D mass discharge rate of magma, MT^{-1}.
Ds ratio of eruption mixture density to atmospheric density.
e radiation emissivity.
$\mathbf{g}$ gravitational acceleration, directed toward $-z$, LT^{-2}.
H elevation of top of eruption column, L.
I specific internal energy, L^2T^{-2}.
k thermal conductivity, $ML\ T^{-3}\ K^{-1}$.
K interphase momentum transfer function, $ML^{-3}T^{-1}$.
K_p ratio of vent exit pressure to atmospheric pressure.
L characteristic length, L.
M Mach number, ratio of flow speed to sound speed.
m ratio of mass of solid phase per unit volume of mixture to mass of gas phase per unit volume of mixture.
p gas pressure, $ML^{-1}T^{-2}$.
Δp characteristic pressure change, $ML^{-1}T^{-2}$.
Pn Rouse number, ratio of particle settling velocity to vertical flow speed.
Pr Prandtl number, ratio of momentum diffusivity to thermal diffusivity.
q intraphase conductive heat transport, MT^{-3}.
R interphase heat transfer, $ML^{-1}T^{-3}$.
r radial distance from symmetry axis, L.
r_s particle radius, L.
R_v vent radius, L.
Ri_m Richardson number, ratio of inertia to buoyancy in terms of erupting mixture properties.
Ry Reynolds number, ratio of inertia to viscous dissipation.
t time, T.
T temperature, K.
ΔT temperature difference between phases $T_s - T_g$, K.
Tg_m thermogravitational parameter, ratio of pressure driving force to buoyancy.
u radial component of velocity, LT^{-1}.
$\mathbf{u}$ velocity vector, LT^{-1}.
$\Delta\mathbf{u}$ slip velocity $\mathbf{u}_g - \mathbf{u}_s$, LT^{-1}.
v axial component of velocity, LT^{-1}.
v_e axial (vertical) velocity component at vent exit plane, LT^{-1}.
w_s terminal or settling velocity of particles, LT^{-1}.
z axial (vertical) distance above vent exit plane, L.
ε Stefan-Boltzmann constant, $MT^{-3}K^{-4}$.
γ ratio of specific heats of gas phase.
θ volume concentration of specified phase.
ν momentum diffusivity or kinematic viscosity, L^2T^{-1}.
ρ material density of specified phase, ML^{-3}.
τ viscous stress tensor, $ML^{-1}T^{-2}$.

Subscripts

atm atmosphere.
dg dusty gas.
e conditions at vent exit plane.
g gas (compressible) phase.
m mixture.
s solid (incompressible) phase.

Acknowledgments. This work is supported by Institutional Supporting Research and Development funds from the U.S. Department of Energy at Los Alamos National Laboratory. Thoughtful reviews by Susan Kieffer, Lionel Wilson, Frank Spera, and Rodney Whitaker are greatly appreciated. Special thanks go to Marty Horn, who adapted the DASH code for volcanic applications, and Francis Harlow and Thomas Cook for help in interpretation of some results. Chick Keller, Wes Meyers, Brook Sandford, and Eric Jones have given strong institutional backing and computer guidance.

REFERENCES

Allen, J. R. L., *Physical Processes of Sedimentation*, 248 pp., Allen and Unwin, London, 1970.
Amsden, A. A., and F. H. Harlow, KACHINA: An Eulerian computer program for multifield fluid flows, *Los Alamos Natl. Lab. Rep., LA-5680*, 1974.
Bacon, C. R., Eruptive history of Mount Mazama and Crater Lake caldera, Cascade Range, USA, *J. Volcanol. Geotherm. Res., 18*, 57–115, 1983.
Beget, J. E., and A. J. Limke, Two-dimensional kinematic and rheological modeling of the 1912 pyroclastic flow, Katmai, Alaska, *Bull. Volcanol., 50*, 148–160, 1988.
Bird, R. B., W. E. Stewart, and E. N. Lightfoot, *Transport Phenomena*, 780 pp., John Wiley, New York, 1960.
Blandford, R. D., and M. F. Rees, A 'twin-exhaust' model for double radio sources, *Mon. Not. R. Astron. Soc., 169*, 395–415, 1974.
Brown, G. L., and A. Roshko, On density effects and large structure in turbulent mixing layers, *J. Fluid Mech., 64*, 775–816, 1974.
Caress, M. E., Volcanology of the Youngest Toba Tuff, Sumatra, M.S. thesis, 175 pp., Univ. of Hawaii, Honolulu, 1985.
Carey, S., and R. S. J. Sparks, Quantitative models of the fallout and dispersal of tephra from volcanic eruption columns, *Bull. Volcanol., 48*, 127–141, 1986.
Carrier, G. F., Shock waves in a dusty gas, *J. Fluid Mech., 4*, 376–382, 1958.
Cas, R. A. F., and J. V. Wright, *Volcanic Successions: Modern and Ancient*, 528 pp., Allen and Unwin, London, 1987.
Chemical Propulsion Information Agency, Joint Army, Navy, NASA, Air Force (JANNAF) handbook of rocket exhaust plume technology, *Publ. 263*, chap. 2, 237 pp., Washington, D. C., 1975.
Criswell, C. W., Chronology and pyroclastic stratigraphy of the May 18, 1980, eruption of Mount St. Helens, Washington, *J. Geophys. Res., 92*, 10,237–10,266, 1987.
Denlinger, R. P., A model for generation of ash clouds by pyroclastic flows, with application to the 1980 eruptions at Mount St. Helens, Washington, *J. Geophys. Res., 92*, 10,284–10,298, 1987.
Druitt, T. H., Vent evolution and lag breccia formation during the Cape Riva eruption of Santorini, Greece, *J. Geol., 93*, 439–454, 1985.
Druitt, T. H., and C. R. Bacon, Lithic breccia and ignimbrite erupted during the collapse of Crater Lake Caldera, Oregon, *J. Volcanol. Geotherm. Res., 29*, 1–32, 1986.
Druitt, T. H., and R. S. J. Sparks, A proximal ignimbrite breccia facies on Santorini, Greece, *J. Volcanol. Geotherm. Res., 13*, 147–171, 1982.
Druitt, T. H., and R. S. J. Sparks, On the formation of calderas during ignimbrite eruptions, *Nature, 310*, 679–681, 1984.
Fisher, R. V., Models for pyroclastic surges and pyroclastic flows, *J. Volcanol. Geotherm. Res., 6*, 305–318, 1979.
Fisher, R. V., and H.-U. Schmincke, *Pyroclastic Rocks*, 472 pp., Springer-Verlag, New York, 1984.
Flaud, J. M., C. C. Peyret, J. P. Maillard, and G. Guelachvili, The H_2O spectrum between 4200 and 5000 cm^{-1}, *J. Mol. Spectrosc., 65*, 219–228, 1977.
Freundt, A., and. H.-U. Schmincke, Lithic-enriched segregation bodies in pyroclastic flow deposits of Laacher See volcano (East Eiffel, Germany), *J. Volcanol. Geotherm. Res., 25*, 193–224, 1985.
Freundt, A., and H.-U. Schmincke, Emplacement of small-volume pyroclastic flows at Laacher See (East Eiffel, Germany), *Bull. Volcanol., 48*, 39–60, 1986.
Hampton, M. A., The role of subaqueous debris flow in generating turbidity currents, *J. Sediment. Petrol., 42*, 775–793, 1972.
Harlow, F. H., and A. A. Amsden, Numerical calculation of multiphase fluid flow, *J. Comput. Phys., 17*, 19–52, 1975.
Hildreth, W., New perspectives on the eruption of 1912 in the Valley

of Ten Thousand Smokes, Katmai National Park, Alaska, *Bull. Volcanol., 49*, 680–693, 1987.
Hirt, C. W., Heuristic stability theory for finite-difference equations, *J. Comput. Phys., 2*, 339–355, 1968.
Horn, M., Physical models of pyroclastic clouds and fountains, M.S. thesis, 125 pp., Ariz. State Univ., Tempe, 1986.
Incropera, F. P., and D. P. DeWitt, *Fundamentals of Heat Transfer*, 819 pp., John Wiley, New York, 1981.
Ishii, R., Y. Umeda, and K. Kawasaki, Nozzle flows of gas-particle mixtures, *Phys. Fluids, 30*, 752–760, 1987.
Jakosky, B. M., Volcanoes, the stratosphere, and climate, *J. Volcanol. Geotherm. Res., 28*, 247–255, 1986.
Kieffer, S. W., Fluid dynamics of the May 18 blast at Mount St. Helens, *U.S. Geol. Surv. Prof. Pap., 1250*, 379–400, 1981.
Kieffer, S. W., Dynamics and thermodynamics of volcanic eruptions: Implications for the plumes on Io, in *Satellites of Jupiter*, edited by D. Morrison, pp. 647–723, University of Arizona Press, Tucson, 1982.
Kieffer, S. W., Factors governing the structure of volcanic jets, in *Explosive Volcanism: Inception, Evolution, and Hazards*, pp. 143–157, National Academy Press, Washington, D. C., 1984.
Kieffer, S. W., and B. Sturtevant, Laboratory studies of volcanic jets, *J. Geophys. Res., 89*, 8253–8268, 1984.
Kite, W. M., Caldera-forming eruption sequences and facies variations in the Bandelier Tuff, central New Mexico, M.S. thesis, 376 pp., Ariz. State Univ., Tempe, 1985.
Liepmann, H. W., and A. Roshko, *Elements of Gasdynamics*, 439 pp., John Wiley, New York, 1957.
Lipman P. W., Caldera-collapse breccias in the western San Juan Mountains, Colorado, *Geol. Soc. Am. Bull., 87*, 1397–1410, 1976.
Marble, F. E., Dynamics of dusty gas, *Annu. Rev. Fluid Mech., 2*, 397–446, 1970.
Morton, B. R., G. I. Taylor, and J. S. Turner, Turbulent gravitational convection from maintained and instantaneous sources, *Philos. Trans. R. Soc. London, Ser. A, 234*, 1–23, 1956.
Norman, M. L., L. Smarr, K. H. A. Winkler, and M. D. Smith, Structure and dynamics of supersonic jets, *Astron. Astrophys., 113*, 285–302, 1982.
Prandtl, L., *The Essentials of Fluid Mechanics*, Blackie, London, 1954.
Reynolds, W. C., and H. C. Perkins, *Engineering Thermodynamics*, 690 pp., McGraw-Hill, New York, 1977.
Riehle, J. R., Calculated compaction profiles of rhyolitic ash-flow tuffs, *Geol. Soc. Am. Bull., 84*, 2193–2216, 1973.
Rose, W. I., and C. A. Chesner, Dispersal of ash in the great Toba eruption, 75 ka, *Geology, 15*, 913–916, 1987.
Rudinger, G., Some properties of shock relaxation in gas flows carrying small particles, *Phys. Fluids, 7*, 658–663, 1964.
Savage, S. B., The mechanics of rapid granular flows, *Adv. Appl. Mech., 24*, 289–366, 1984.
Settle, M., Volcanic eruption clouds and the thermal output of explosive eruptions, *J. Volcanol. Geotherm. Res., 3*, 309–324, 1978.
Sheridan, M. F., Emplacement of pyroclastic flows: A review, *Spec. Pap. Geol. Soc. Am., 180*, 125–136, 1979.
Sparks, R. S. J., Grain size variations in ignimbrites and implications for the transport of pyroclastic flows, *Sedimentology, 23*, 147–188, 1976.
Sparks, R. S. J., The dimensions and dynamics of volcanic eruption columns, *Bull. Volcanol., 48*, 3–16, 1986.
Sparks, R. S. J., and G. P. L. Walker, The ground surge deposit—A third type of pyroclastic rock, *Nature Phys. Sci., 241*, 62–64, 1973.
Sparks, R. S. J., and G. P. L. Walker, The significance of vitric-enriched air-fall ashes associated with crystal-enriched ignimbrites, *J. Volcanol. Geotherm. Res., 2*, 329–341, 1977.
Sparks, R. S. J., and L. Wilson, A model for the formation of ignimbrite by gravitational column collapse, *J. Geol. Soc. London, 132*, 441–451, 1976.
Sparks, R. S. J., and L. Wilson, Explosive volcanic eruptions, V, Observations of plume dynamics during the 1979 Soufriere eruption, St. Vincent, *Geophys. J. R. Astron. Soc., 69*, 551–570, 1982.
Sparks, R. S. J., S. Self, and G. P. L. Walker, Products of ignimbrite eruption, *Geology, 1*, 115–118, 1973.
Sparks, R. S. J., L. Wilson, and G. Hulme, Theoretical modeling of the generation, movement, and emplacement of pyroclastic flows by column collapse, *J. Geophys. Res., 83*, 1727–1739, 1978.
Stewart, H. B., and B. Wendroff, Two-phase flow: Models and methods, *J. Comput. Phys., 56*, 363–409, 1984.
Taylor, G. A., The 1951 eruption of Mount Lamington, Papua, *Aust. Bur. Min. Resour. Geol. Geophys. Bull., 38*, 1–117, 1958.
Tennekes, H., and J. L. Lumley, *A First Course in Turbulence*, 300 pp., MIT Press, Cambridge, Mass., 1972.
Valentine, G. A., Stratified flow in pyroclastic surges, *Bull. Volcanol., 49*, 616–630, 1987.
Valentine, G. A., and R. V. Fisher, Origin of layer 1 deposits in ignimbrites, *Geology, 14*, 146–148, 1986.
Walker, G. P. L., Origin of coarse lithic breccias near ignimbrite source vents, *J. Volcanol. Geotherm. Res., 25*, 157–171, 1985.
Walker, G. P. L., L. Wilson, and E. L. G. Bowell, Explosive volcanic eruptions, I, The rate of fall of pyroclasts, *Geophys. J. R. Astron. Soc., 22*, 377–383, 1971.
Walker, G. P. L., S. Self, and P. C. Froggatt, The ground layer of the Taupo ignimbrite: A striking example of sedimentation from a pyroclastic flow, *J. Volcanol. Geotherm. Res., 10*, 1–11, 1981.
Weast, R. C. (Ed.), *CRC Handbook of Chemistry and Physics*, 60th ed., p. E393, CRC Press, Boca Raton, Fla., 1979.
Wilson, C. J. N., The role of fluidization in the emplacement of pyroclastic flows: An experimental approach, *J. Volcanol. Geotherm. Res., 8*, 231–248, 1980.
Wilson, C. J. N., The role of fluidization in the emplacement of pyroclastic flows, 2, Experimental results and their interpretation, *J. Volcanol. Geotherm. Res., 20*, 55–84, 1984.
Wilson, C. J. N., The Taupo eruption, New Zealand, II, The Taupo ignimbrite, *Philos. Trans. R. Soc. London, Ser. A, 314*, 229–310, 1985.
Wilson, C. J. N., and G. P. L. Walker, Ignimbrite depositional facies: The anatomy of a pyroclastic flow, *J. Geol. Soc. London, 139*, 581–592, 1982.
Wilson, C. J. N., and G. P. L. Walker, The Taupo eruption, New Zealand, I, General aspects, *Philos. Trans. R. Soc. London, Ser. A, 314*, 199–228, 1985.
Wilson, L., Explosive volcanic eruptions, III, Plinian eruption columns, *Geophys. J. R. Astron. Soc., 45*, 543–556, 1976.
Wilson, L., and J. W. Head, Morphology and rheology of pyroclastic flows and their deposits, and guidelines for future observations, *U.S. Geol. Surv. Prof. Pap., 1250*, 513–524, 1981.
Wilson, L., and G. P. L. Walker, Explosive volcanic eruptions, VI, Ejecta dispersal in Plinian eruptions: The control of eruption conditions and atmospheric properties, *Geophys. J. R. Astron. Soc., 89*, 657–679, 1987.
Wilson, L., R. S. J. Sparks, T. C. Huang, and N. D. Watkins, The control of volcanic column heights by eruption energetics and dynamics, *J. Geophys. Res., 83*, 1829–1836, 1978.
Wilson, L., R. S. J. Sparks, and G. P. L. Walker, Explosive volcanic eruptions, IV, The control of magma properties and conduit geometry on eruption column behavior, *J. Geophys. J. R. Astron. Soc., 63*, 117–148, 1980.
Wilson, L., H. Pinkerton, and R. Macdonald, Physical processes in volcanic eruptions, *Annu. Rev. Earth Planet. Sci., 15*, 73–95, 1987.
Wohletz, K. H., T. R. McGetchin, M. T. Sandford II, and E. M. Jones, Hydrodynamic aspects of caldera-forming eruptions: Numerical models, *J. Geophys. Res., 89*, 8269–8286, 1984.
Woods, A. W., The fluid dynamics and thermodynamics of eruption columns, *Bull. Volcanol., 50*, 169–193, 1988.
Wright, J. V., The Rio Caliente ignimbrite: Analysis of a compound intraplinian ignimbrite from a major late Quaternary Mexican eruption, *Bull. Volcanol., 44*, 189–212, 1981.
Wright, J. V., and G. P. L. Walker, The ignimbrite source problem: Significance of a co-ignimbrite lag-fall deposit, *Geology, 5*, 729–732, 1977.
Wright, J. V., and G. P. L. Walker, Eruption, transport and deposition of ignimbrite: A case study from Mexico, *J. Volcanol. Geotherm. Res., 9*, 111–131, 1981.

K. H. Wohletz, Mail Stop D462, Geology-Geochemistry Group ESS-1, Earth and Space Sciences Division, Los Alamos National Laboratory, Los Alamos, NM 87545.

G. A. Valentine, Mail Stop F665, Geoanalysis Group ESS-5, Earth and Space Sciences Division, Los Alamos National Laboratory, Los Alamos, NM 87545.

(Received May 3, 1988;
revised August 10, 1988;
accepted October 4, 1988.)